Politecnico di Milano

Scuola di Ingegneria dei Sistemi

Corso di Laurea Magistrale in Ingegneria Fisica

Process development for a metallic spin-flip based laser fabrication

Relatore

Prof. Marco Finazzi

Laureando

Roberto Lo Conte (mat. 752094)

Correlatore

Dr. Adrian Iovan (KTH-Stoccolma)

A.A. 2011/2012

Abstract

Integration of novel magnetic nanodevices into conventional electronic circuits is the main aim of research and development in the new field referred to as Spintronics. Spin-valves and Magnetic Random Access Memory (MRAM) are examples of already developed spintronic devices. In this work the aim is to develop a fabrication process for a novel spin laser device. Exploiting the high electron density combined with the intrinsic energy splitting between the two spin sub-bands in a ferromagnetic metal makes it possible in principle to obtain a metallic laser with an high optical gain. The emission frequency would be determined by the exchange energy spitting for a given ferromagnet used in fabricating the laser device. A theoretical description as well as experimental results indicating spin-flip photon emission processes for single magnetic point contacts have been reported recently. Based on these results, a spin laser device is designed and fabricated – the main focus of this work. A disk-shaped resonator containing an array of magnetic point contacts was patterned using a colloidal lithography process combined with conventional photolithography. Using colloidal lithography allowed to pattern a SiO_2/Al-mask with a self-assembled hexagonal nanostructure. The mask consisted of an array of apertures with diameter 10-15 nm separated by 200 nm. The holes are subsequently filled with FeCr and Fe so that magnetic point contacts of size about 10 nm were obtained. The micrometer scale disk-shaped resonators enclosing the point contact arrays were patterned by optical lithography. Resonators with diameters from 10 µm to 50 µm were fabricated. Four-point electrical measurements have been done on the integrated devices, with contact pads to resonators containing point contact arrays. The device resistance R as well as their differential resistance dV/dI have been measured. About 10% of the samples showed excitations in R and dV/dI very similar to the ones measured in previous works on single magnetic PCs. Current-Induced Hysteretic Switching as well as Current –Induced Spin-Transfer Torque were thus detected in the fabricated arrays. Moreover, in a few samples large excitations at high bias voltages were measured. They are characterized by a 2-fold increase in the resistance, with a threshold character in bias voltage, which is typical of laser devices. A direct confirmation of lasing in the devices fabricated will be future optical measurements in the terahertz range, where the spin-flip radiation is expected.

Estratto di tesi

Nel seguente manoscritto viene descritto il lavoro di ricerca svolto dall'autore presso il dipartimento di Fisica Applicata del Royal Institute of Technology (KTH) di Stoccolma (Svezia) durante il periodo che va da Dicembre 2011 a Maggio 2012. Il principale obiettivo del lavoro sperimentale effettuato nel laboratorio di Nano-Fabbricazioni della suddetta Università era lo sviluppo di un processo per la fabbricazione di un nuovo tipo di laser, basato su materiali metallici ferromagnetici. L'autore ha prima imparato ad eseguire un pre-esistente processo adibito a tale scopo e poi ha continuato nello sviluppare ulteriormente tale processo.

I due pilastri su cui si basa tale lavoro sperimentale sono: da una parte, il nuovo campo di ricerca della Fisica dello Stato Solido denominata Spintronica; dall'altra, la tecnica dei Point-Contact (PC). Col termine Spintronica si indica quel ramo della Fisica in cui si studiano le proprietà di nano strutture magnetiche, in cui il momento magnetico di spin dell'elettrone gioca un ruolo fondamentale. Invece la tecnica dei Point-Contact si basa sul far scorrere corrente elettrica tra due metalli connessi tra di loro tramite una nanometrica strizione (10-20 nm in diametro), il Point-Contact per l'appunto.

L'investigazione e la conseguente teoria dei Point-Contact è stata sviluppata negli ultimi cinquant'anni. Ciò che è importante dire è che a seconda del rapporto tra la dimensione laterale d del PC e il libero cammino medio (l.c.m.) degli elettroni, il contatto può lavorare in tre differenti regimi: ballistic, diffusive e thermal. Dal primo all'ultimo caso il l.c.m. risulta essere molto più grande, comparabile o molto più piccolo di d. Nel caso in cui si è nel regime ballistic gli elettroni possono passare da una parte all'altra del PC senza perdere energia. Questo ci dà la possibilità di iniettare elettroni caldi dall'altra parte del PC, ragion per cui i PC vengono utilizzati in questo progetto. La capacità di iniettare elettroni caldi offre la possibilità di pompare un metallo e creare al suo interno una inversione di popolazione.

Dall'altra parte, era importante capire quali erano i meccanismi alla base dell'effetto laser. Prima di tutto è stato eseguito uno studio di articoli (teorici e sperimentali) precedentemente pubblicati, in cui la fisica alla base di tale dispositivo viene illustrata. In tali articoli viene dimostrata la possibilità teorica di ottenere la produzione di fotoni tramite decadimenti "spin-flip" di elettroni in un singolo PC. Più nello specifico, una corrente altamente spin-polarizzata viene iniettata da uno strato ferromagnetico (FeCr) in un ago di rame con una punta nanometrica (10-20 nm in diametro). Applicando un campo magnetico esterno, viene indotto uno Zeeman-splitting nella banda di conduzione del rame tra gli elettroni con spin opposto. Ponendosi nella opportuna configurazione è possibile pompare la banda con stati energetici superiori, così che ad un certo livello di pompaggio l'inversione di popolazione viene ottenuta. In tutto questo gioca un ruolo fondamentale la dipendenza che ha la conducibilità degli elettroni nel ferromagnete rispetto al momento magnetico di spin degli elettroni stessi. Poi, tramite il decadimento di elettroni dalla banda superiore alla banda inferiore, con conseguente inversione del loro momento di spin, vengono emessi fotoni. Negli stessi articoli viene anche riportata la dimostrazione sperimentale dell'emissione di fotoni, la cui energia è in risonanza con la separazione indotta tra le due bande di conduzione. Gli autori spiegano che in corrispondenza dell'emissione di fotoni si ha un incremento della resistenza del PC, incremento che loro hanno misurato nei loro esperimenti.

Partendo da questa base iniziale, nasce l'idea di un processo per la fabbricazione di un laser basato su di un array di PC magnetici. L'idea è quella di confinare tale array, che risulterà il materiale attivo del dispositivo, in una matrice dielettrica, tra due contatti metallici. La prima proposta è quella di un risonatore cilindrico (con diametro nell'ordine delle decine di micron) in cui

la radiazione e.m. viene confinata verticalmente dai due contatti metallici e lateralmente dal salto d'indice di rifrazione tra lo strato dielettrico contenente i PC e l'aria. I due contatti metallici sono connessi elettricamente tramite l'array di PC, i quali risultano essere elettricamente in parallelo. In questo tipo di risonatore: la lunghezza d'onda della luce emessa viene fissata dalla separazione in energia tra le due bande di conduzione; mentre il modo ottico viene selezionato dal diametro del risonatore. Infine è importante sottolineare che possono essere impiegati anche PC completamente magnetici, composti cioè da due metalli ferromagnetici. In questo caso lo splitting tra le due bande di conduzione sarebbe dovuto all'exchange field intrinseco del ferromagnete. Non è più necessario applicare un campo magnetico esterno, rendendo il dispositivo più adatto per applicazioni in circuiti integrati.

Nell'esecuzione del processo di fabbricazione di questo innovativo dispositivo, differenti macchine e strumenti sono stati utilizzati. Sistemi di Spattering e Electron Beam Evaporation sono stati utilizzati per la deposizione di film sottili. Mentre, per i processi di patterning sono stati utilizzati il Reactive Ion Etching e l'Argon Ion Milling, insieme alla Fotolitografia ed alla Litografia Colloidale. Quest'ultima è forse la tecnica che più di tutte caratterizza questo processo di fabbricazione, essendo impiegata nel processo di patterning dei PC e considerando l'importanza che tali nano contatti hanno nel dispositivo.

L'intero processo può essere suddiviso in quattro parti principali: patterning del bottom-contact; patterning dell'array di PC magnetici; patterning del risonatore e patterning del top-contact. La struttura di partenza è un multilayer metallico, in cui principalmente abbiamo uno strato di Alluminio di 150nm e uno strato isolante in superficie di SiO_2 di 15nm. Il multilayer è stato depositato su di un wafer di Silicio.

La prima fase è il patterning del bottom-contact. Un primo step di fotolitografia, seguito da un processo di argon ion milling permette di ottenere una struttura larga 250µm, lunga circa 6mm e alta circa 180nm. Dopo il processo di etching, tutto il multilayer metallico è stato eliminato, così che il contatto metallico ottenuto è elettricamente isolato.

La seconda fase è il patterning dell'array di PC magnetici, in cui la tecnica di Litografia Colloidale viene impiegata. Sulla superficie del campione viene depositato tramite spin-coater una soluzione acquosa di nano sfere di Polistirene di 200nm in diametro, in modo da ottenere un monolayer auto-assemblato di tali nano particelle. Le particelle si dispongono sulla superficie del campione in configurazione hexagonal-close-packed. Tramite un processo di RIE con ossigeno, le nano particelle vengono ridotte in dimensione fino ad un diametro medio di circa 15nm ed un'altezza di qualche nm superiore. Tramite una deposizione di Al, uno strato metallico di 15nm va a racchiudere in se le particelle. A questo punto, una serie di processi di etching (RIE) con ossigeno prima e argon poi rimuove completamente le particelle, così da ottenere il trasferimento della struttura esagonale nel metallo. Poi, un ultimo step di RIE con CF4 permette di generare dei canali attraverso lo strato di SiO_2 con dei diametri di circa 15nm, fino al raggiungimento dello strato metallico sottostate. Infine, uno strato di 10nm di FeCr ed uno di 15nm di Fe vengono depositati tramite spattering, in modo da ottenere il patterning dell'array di PC magnetici desiderato. Con questi materiali, in cui si ha che la temperatura di Curie dello strato di FeCr è circa 500°C, la frequenza di emissione può essere stimana intorno a 10THz.

La terza fase è il patterning del risonatore ottico. Come nella prima fase, uno step di fotolitografia e uno di ion milling vengono eseguiti in cascata. In questo modo una linea di strutture cilindriche (o semi-cilindriche, visto che due differenti geometrie per il risonatore sono state sperimentate durante

lo sviluppo e l'ottimizzazione del processo) contenenti il materiale attivo vengono sagomate al di sopra del bottom-contact.

Infine vengono patternati i top-contact. Una linea di contatti metallici vengono depositati sul campione, tramite un ultimo step di fotolitografia, deposizione di 200nm di Al e conseguente lift-off. In questo modo una linea di differenti dispositivi (con diametri che vanno da 10 µm a 50 µm) su di uno stesso chip sono stati fabbricati, ognuno dei quali può essere connesso elettricamente ad un circuito esterno indipendentemente dagli altri. A questo punto il campione è pronto per le misure elettriche.

Sul campione sono state eseguite misure elettriche con la configurazione a 4 punti. Un circuito elettrico fornito di sistema Lock-in è stato utilizzato in modo da poter eseguire misure della resistenza R del dispositivo ed anche della sua resistenza differenziale dV/dI. Tutti gli stumenti erano collegati tramite cavi IEEE-488 ad un computer, dove i dati venivano letti e conservati. L'acquisizione dei dati avveniva tramite un software che lavorava in una ambientazione Lab-View. In questo modo si otteneva una completa caratterizzazione elettrica del dispositivo, compresa la sua caratteristica I-V (IVC). Le misure sono state effettuate sia a temperatura ambiente che a 77K (Azoto liquido), senza però riscontrare differenze notevoli tra i due casi.

Dalle misure elettriche si è subito visto, nella maggior parte dei dispositivi indagati, che le caratteristiche R-I e soprattutto dV/dI-I avevano la tipica forma parabolica riscontrata da altri ricercatori nelle misure eseguite su singoli PC. Questa era una prova chiara che l'array di PC in parallelo funzionava. Questo era supportato anche dal fatto che la resistenza totale del dispositivo R (circa 0.1-0.01Ω) era 100-500 volte inferiore a quella di un singolo PC con diametro nel range di 10nm-20nm, anche se questo accadeva in un numero più ristretto di dispositivi indagati. Passando poi alla ricerca di prove del carattere magnetico dei PC, in un 10% dei dispositivi si sono misurate delle eccitazioni nelle suddette caratteristiche, alcune delle quali sembrerebbero avere un tipico stampo magnetico. Come mostrato già in precedenti articoli su singoli PC magnetici: un effetto di Spin-Trasfer Torque è caratterizzato da un picco nella dV/dI-I; mentre un Current-Induced Hysteretic Switching risulta in un ciclo di isteresi all'interno delle due caratteristiche R-I e dV/dI-I. Soprattutto quest'ultimo è stato più volte misurato, in differenti dispositivi. Questo è una prova che i PC lavorano effettivamente come PC magnetici, e che una sorta di allineamento tra le due magnetizzazioni nei due materiali magnetici c'è. Infine, solo in pochissimi dispositivi e solo nell'ultimo periodo sono state rilevate delle eccitazioni in R e dV/dI a più alti livelli di bias, con caratteristiche mai viste prima in precedenti lavori. Una forte non linearità in IVC viene generata ad un certo valore di V, e persiste per tutti i valori di V superiori a quel valore di soglia. Sembrerebbe un tipico fenomeno fisico contraddistinto da un effetto di threshold, come accade in un laser per l'appunto.

In conclusione, prima di tutto un processo per il patterning di un array di PC con diametri di circa 10nm-15nm , basato sulla tecnica della Litografia Colloidale, è stato sviluppato in modo soddisfacente. I dispositivi caratterizzati da un array magnetico hanno mostrato, nel 10% dei casi, dei tipici effetti magnetici, come cicli di isteresi nelle caratteristiche R-I e dV/dI-I. Questo fa pensare che la configurazione magnetica dei PC sia quella giusta per l'ottenimento dell'effetto laser desiderato. Solo recentemente, ed in pochissimi dispositivi, sono state misurate delle non linearità in IVC che sembrerebbero essere collegate in modo diretto con la produzione di luce all'interno dei dispositivi. Ad ogni modo, servono ulteriori misure per chiarire meglio quale sia la vera origine di tali non linearità. Solo delle misure ottiche (che verranno eseguite dopo la stesura di questo manoscritto) in cui verrà misurata della radiazione e.m. emessa da uno dei dispositivi, nel range dei terahertz,

potranno dimostrare l'effettiva produzione di fotoni tramite il meccanismo sopraindicato.

Contents

Chapter 1

Introduction

The aim of this manuscript is to describe in a complete way the research work I did as master thesis project at the Applied Physics department of the Royal Institute of Technology (Kungliga Tekniska Högskolan - KTH) in Stockholm (Sweden). The final target of the project directed by Prof. Korenivski, my examiner and chief of the Spintronics group at KTH is to obtaine a process for the fabrication of a metallic spin-flip based laser. My work has consisted mostly in learning a developed process by my advisor Dr. Adrian Iovan for the patterning of the proposed device and improving it further. In this document I will start with a brief introduction about the branch of physics where it is possible to allocate my project, in order to give the reader an idea of what is the manuscript about. In the next chapter I will illustrate the theoretical background which lies behind the proposed device. In Chapter 3 I will describe all the main instruments I have been using during the last six months for the patterning process. Chapter 4 will be dedicated to the description of the whole process for the fabrication of the device, with a few words about some changes which have been executed in order to improve the process itself and/or the characteristics of the device. In the fifth chapter I will illustrate the electrical measurements set-up I used to characterize my samples and the respective results. Finally, in Chapter 6 there will be my conclusions/considerations about the obtained results.

1.1 Spintronics

The main field of research in which we could allocate the work I did is the new field of Spintronics. Spintronics means Spin Electronics, and how it is easy to understand the main target of this field is to exploit not only the electrical charge but also and mainly the intrinsic spin angular momentum of electrons. In this way is possible to built a new kind of electronics which is based on the spin of electrons. For example, it is possible to exploit the fact that the resistance of a magnetic nanostructure is function of its magnetic configuration, like in the case of the Giant Magnetoresistance effect (GMR). After the discovery of GMR, independently by physicists Peter Grünberg and Albert Fert in 1988[1, 2], the research about the new opportunities offered by the spin of electrons in the obtaining of new kind of electronic devices started to increase rapidly. Nowadays spintronic devices are already on the high-technology market, like for examples the read-out head of magnetic hard disks, which exploit the GMR and the Current-Driven Pseudo-Torque effects in order to read

and/or write data-bits on the hard disk. On the other hand, other devices are still in elaboration, but almost ready to get into the market, like for example the Magnetic Random Access Memory (MRAM), which IBM is still working on after more than ten years of research and development [3]. Actually also the MRAM has already on the market, but it still needs further improvements (for example, an higher density of memory cells) in order to compete with existing memories.

1.2 Point-Contacts

The other centerpiece at the base of this project are the Point-Contacts (PCs). A point-contact is a small constriction, a few nanometers large, between two conductors. It can consist of one (homocontact) or two materials (heterocontact). How I will illustrate more in depth in the next chapter, since the lateral dimension of the PC is smaller than the electron mean free path the I-V characteristic (IVC) results to be nonlinear, and its second derivative turns out to be proportional to the spectrum of the conduction electron-quasiparticle interaction. This has given the opportunity of developing a new kind of spectroscopy in the field of Solid State Physics, the Point-Contacts Spectroscopy (PCS)[4]. According to this, we could think to exploit I-V characteristics of our sample in order to obtain some evidences of the characteristic threshold phenomenon that is supposed to occur in case of light generation by magnetic PCs. Then, comparing these data with the ones coming out from optical measurements it could be possible to better analyze the I-V curves and the optical spectrum at the same time.

In this project the idea is to use an array of magnetic PCs as active material of a new kind of laser, a metallic spin-flip based laser. My work consisted in getting familiar with an existing patterning process of a metallic spin-flip Terahertz laser based on magnetic point contacts and improving it further. The dimensions required for the contacts into such device are below 20 nm in diameter and this is a challenge for standard patterning techniques. The colloidal lithography in combination with photo-lithography will be employed into the development. Through the manuscript I will have the opportunity to illustrate and analyze all the technical features of this project.

Chapter 2

Theoretical background

2.1 Point contacts theory

2.1.1 Metallic point contacts

The investigation about metallic point contacts started already in the middle of the 60's of the last century. In the 1965 Sharvin [4, p.5] gave a theoretical description of the resistance of *ballistic* contacts where the mean free path l of electrons is larger then the dimension d of the constriction. Since the beginning of the 1970's until now I. K. Yanson[1] studied in a systematic way point contacts made of almost all the existing metals and superconductors. His work is reported and discussed in depth in the book *"Point-Contacts Spectroscopy"*, written by Yu. G. Naidyuk and him and published in the 2005[4]. My knowledge about the topic comes mainly from this book and some published scientific papers[5, 6].

Sharvin's approach was quite simple: he imagines a ballistic point contact as a small metallic connection between two metallic plates separated by a thin insulator interlayer through an hole of diameter d in the insulator (Fig.2.1). Applying a voltage to the contact, an electron passing the aperture from one side to the other has a gain in speed δv proportional to the applied voltage: $\delta v = eV/p_F$, where e is the electron charge, V is the applied voltage and p_F is the Fermi momentum. The current I we obtain through the contact is: $I \simeq e(\pi d^2/4)n\delta v = (\pi d^2/4)(ne^2/p_F)V$, where n is the electron denisity into the metal. According to Drude's model of metals the resistivity is given by $\rho = p_F/ne^2l$, that gives us the following expression for the contact resistance: $R \simeq 4\rho l/\pi d^2$. After an integration over all the possible angles Sharvin's expression for the resistance of a ballistic circular contact results

$$R_{Sh} = \frac{16\rho l}{3\pi d^2}. \tag{2.1}$$

An expression for the resistance in the opposide case $d \gg l$ was already given by Maxwell (1904) [4, p.6]:

$$R_M = \frac{\rho}{d}. \tag{2.2}$$

[1] Yanson and his research group work at the Point-Contact-Spectroscopy Department of B.Verkin Institute for Low Temperature Physics and Engineering of the National Academy of Science of Ukraine in Kharkiv, Ukraine.

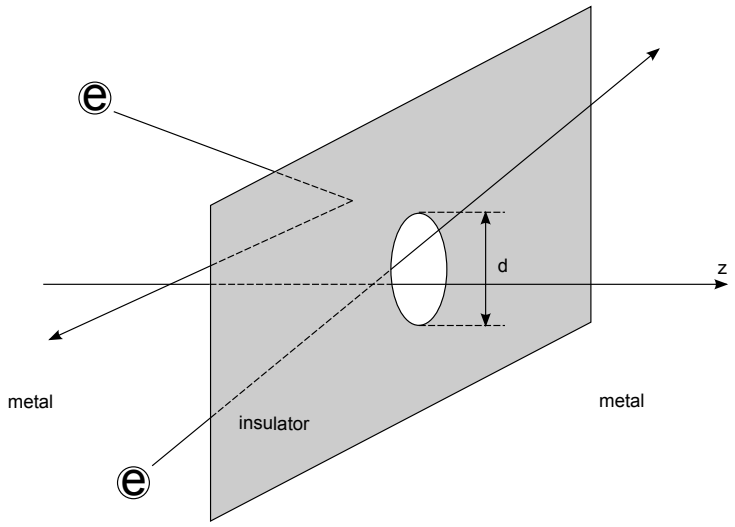

Figure 2.1: *Commonly used model of a ballistic point contact consisting of an orifice with diameter d in an insulating plane between two metallic plates, with trajectories of electrons.[4]*

These two formulas gives us basic models for the two extreme cases of electric transport regime in point contacts, and we can join them in order to model a point contact in all his three working regimes: *ballistic*, *diffusive* and *thermal* (later in the chapter it will be clearer which are the parameters that characterize each regime).

Looking to the nonlinearities present in the IVC of PCs, it has been understood that they are connected to the typical phonon-excitation energies of the metals under investigation. More exactly, the second derivative $d^2V/dI^2(V)$ of the I-V curve is proportional to the electron-phonon interaction function $\alpha^2F(\omega)$, that is given by the convoluted product between the phonon density of state *F(ω)* and the squared matrix element of the electron-phonon interaction α^2. A rapid and approximate way to explain why this proportionality between $d^2V/dI^2(V)$ and $\alpha^2F(\omega)$ is to describe the resistance of the contact as the sum of Sharvin's resistance and Maxwell's resistance, in order to take into account the scattering events the electrons experience into the constriction:

$$R \simeq \frac{16\rho l}{3\pi d^2} + \frac{\rho}{d}. \tag{2.3}$$

The second therm of (2.3) takes into account the contribution to the total resistance coming from the electron-phonon scatterings. It the limit $l > d$, this second therm results to be a small correction to the ballistic Sharvin expression, so it is possible to rewrite (2.3) as a Taylor's expansion at the first order in d/l

$$R \simeq R_{Sh}(1 + \frac{3\pi d}{16l}) = R_{Sh}(1 + \frac{3\pi d}{16 v_F \tau}). \tag{2.4}$$

An energy-dependent scattering time $\tau(eV) = l(eV)/v_F$ gives us a voltage dependent resistance *R(V)*. Finally, adopting Grimvall's expression [4, p.9] for the time of phonon-generation by a nonequilibrium electron at energy eV above the Fermi energy, we have

$$1/\tau_{el-ph}(eV) = \frac{2\pi}{\hbar}\int_0^{eV}\alpha^2(\epsilon)F(\epsilon)d\epsilon \tag{2.5}$$

and making the derivative of (2.4) we get[4]

$$\frac{dR}{dV}(\propto \frac{d^2V}{dI^2}) \simeq R_{Sh}\frac{3\pi^2 ed}{8\hbar v_F}\alpha^2 F(eV). \tag{2.6}$$

This is a rough extimation, but it comes out clearly from it the proportionality between the second derivative of the I-V characteristic and the electron-phonon interaction function. This discovery is the starting point of the new spectroscopic technique known today as Point-Contact Spectroscopy (PCS), a very powerful tool for the investigation of the quasiparticle-excitations (like phonons and magnons) in all the metals and superconductors. All the experimental results obtained by Yanson in the field of PCS are reported in his book[4], a suggested reading for who would like to go more in depth into the PCS technique and the results gotten about all the investigated conductive materials.

Even if the previous explanation for the PCS is clear and simple to follow and understand, it is only a phenomenological approach to the problem. A more complite theory, based on the solution of the Boltzmann equation for the poin-contact geometry, was developed by Kulik [4, pp.17-19], and it confirmes the equation (2.6). The current density j into the PC in the z-direction (the longitudinal axis of the PC, with its origine in the center of the PC)is given by

$$j_z = 2e\sum_k (v_k)_z f_k(\epsilon) \tag{2.7}$$

where $f_k(\epsilon)$ is the nonequilibrium Fermi-Dirac distribution function, that in the contact center reduses to $f_{z=\pm 0}(\epsilon) = (\exp(\frac{\epsilon-\epsilon_F \pm eV/2}{K_B T})+1)^{-1}$ and $\mathbf{v}_k$ is the Fermi velocity. Substituting the summation over all $\mathbf{k}$ values in (2.7) with an integration over all energy values ϵ and angles Ω we get

$$j_z = e\int_{\epsilon_F - eV/2}^{\epsilon_F + eV/2} d\epsilon \int f(\epsilon)v_z(\epsilon)N(\epsilon)\frac{d\Omega}{4\pi}, \tag{2.8}$$

with $d\Omega$ as differential solid angle and $N(\epsilon)$ as electronic density of states. By solving the integral in (2.8) we get again Sharvin's resistance [4, p.19], wich can be expressed also as:

$$R_{Sh} = \frac{16\rho l}{3\pi d^2} = \frac{16R_q}{(k_F d)^2}, \tag{2.9}$$

where $R_q = 1/G_0 = h/2e^2 \simeq 12.9\text{k}\Omega$, and G_0 is the conductance quantum. This makes possible to extract the diameter of a PC in the ballistic regime by measuring the resistance at zero bias R_0. For example, in the case of copper, $d \approx 30/\sqrt{R_0[\Omega]}\text{nm}$[4].

Passing through the constriction, electrons gain an excess energy eV. This accumulated energy can be lost in a scattering event generating quasiparticle excitations (mainly phonons but also magnetic excitation, like spin-waves or Kondo scattering in presence of paramagnetic impurities into normal metals). When scattered, electrons go back in the other direction, giving a modified net

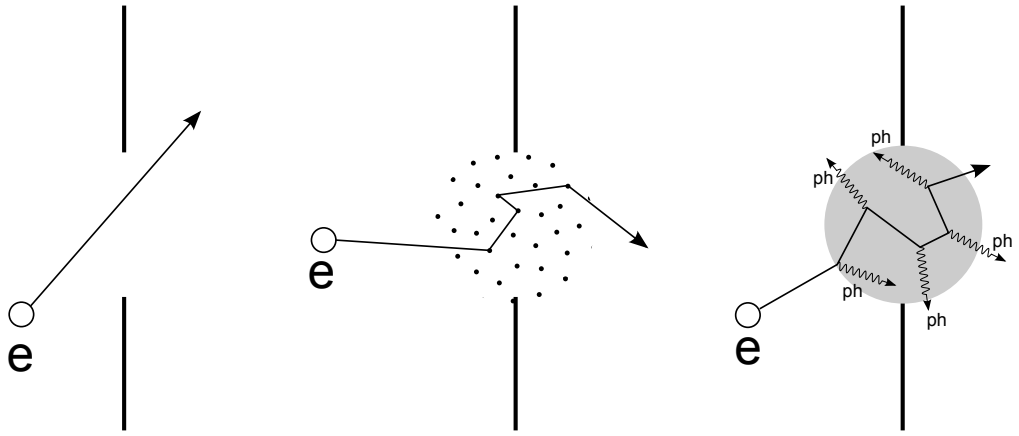

Figure 2.2: *The three different regimes for electrons transport in a point contact: ballistic, diffusive and thermal regime. ph represents a phonon.[4]*

current in the PC. This is the origin of the nonlinearity into the IVC and of the peaks into the second derivative of it.

How said briefly before, the electric transport in PCs can occur in three different regimes. It depends on the relation existing between the elastic l_{el}(that means with energy consevation) and inelastic l_{in}(with energy dissipation) mean free paths of electrons and the point-contact size d (see Fig.2.2). In the case where l_{el},$l_{in} \gg d$ we have a PC working in the ballistic regime; when $l_{el} \ll d \ll \sqrt{l_{in} l_{el}}$ we are in the duffusive regime; finally when l_{el}, $l_{in} \ll d$ the PC is in the thermal regime. If in the thermal regime it is almost impossible to carry out PCS, it is not completely forbidden to do it on PCs working in the diffusive regime. This means that PCS can be applied not only to perfect clean metals, but also to alloys and compounds of different metals. The condition to be respected is that the inelastic relaxation length during the diffusion motion of electrons in the contact $\Lambda = \sqrt{l_{el} l_{in}/3} > d$ [4, p. 26]. For this case, an interpolation formula for the contact resistance was derived by Wexler [4, p.26]in the 1966:

$$R_{PC}(T) = \frac{16\rho l}{3\pi d^2} + \beta \frac{\rho(T)}{d}, \tag{2.10}$$

where β has a value close to the unity at the diffusive regime. By differentiating (2.10) it is possible to obtain an expression for the contact size

$$d = \frac{d\rho/dT}{dR_{PC}/dT}, \tag{2.11}$$

which gives the opportunity for estimating d.

In conclusion, the mean free paths of electrons in metals depend on electrons' energy. When this energy reaches the energy at which there are many phonon modes the mean free paths have rapid variations, they suddenly decrease. Due to the direct relation between the scattering time $\tau(eV) \propto l$ and the second derivative of the measured I-V curve given by the second therm in (2.10) (see (2.4)-(2.6)), at sudden decreases in the mean free path correspond increases (peaks) in $\mathrm{d^2V/dI^2(V)}$. This is the core of PCS theory, even if there are many other secondary phenomena that should be analyzed

more in depth to have a complite overview of all the possibilities and the limitations of this technique. For the understandig of this exposition this brief presentation should be enough.

2.1.2 Magnetic point contacts

In the implementation of the novel device described in this document, magnetic point contacts have been used. An array of magnetic heterocontacts have been obtained at the interface between two magnetic materials. The patterning of the array has been made possible by a new colloidal lithography technique, which will be described in the chapter focused on the sample-preparation process. The theory of heterocontacts is the same of the normal point contacts presented before, with some small variations. In this case we have two different materials that form the PC, this means that they both give a contribution to the total resistance. An axpression for this resistance is [4, p. 31]

$$R_{PC}(T) = \frac{16\rho l}{3\pi d^2} + \frac{\rho_1(T) + \rho_2(T)}{2d}, \tag{2.12}$$

which is the same equation presented before to describe a homocontact, but with the contribution to the "scattering" therm from both the materials. The two different parts of the PC contribute both also to the total scattering spectrum, that in our case is characterized by phonons excitation as well as magnons excitation and probably photons emission. For this reasons lots of I-V measurements have been conducted on different samples, at room as well as at liquid nitrogen temperature, trying to find some evidences of the desired lasing effect in the form of nonlinearities (see Ch. 5).

The PCs technique is critical for the injection of hot electrons from one side of the constriction to the other, in order to generate a population inversion in the second material and so a photons emission [5], and for that it is very important they work in the ballistic or at least in the diffusive regime (see Sec. 2.2). So, the target was to obtain PCs with size $d \simeq 20 - 10$ nm. More precise reasons on why a such kind of PCs have been chosen for this project will be discussed in the last part of this chapter, where the theory of the laser effect will be exposed.

2.2 Spin-dependent transport

When an electron moves into a metal, it can experience scattering phenomena due to the presence of thermal phonons into the metal. This is tipical for all the metallic materials. When the metal is a ferromagnetic material, electrons can experience scattering with magnons, spin-waves given by the coherent oscillation of the atomic spins into the metal. Exactly like in the case of electron-phonon scattering, also in scattering with magnons the momentum of the electrons is changed, resulting in an additional resistivity for the conduction-electrons. So, when we speak about ferromagnets we have to keep in mind that the total resistance of the material is affected by the intrinsic magnetic configuration inside the metal. To better understand what this actually means is necessary to go more in depth and see how is made the Density Of States (DOS) of a ferromagnet.

In ferromagnets like Fe, Co and Ni the intrinsic magnetization is due to the 3d-electrons localized to the atoms. When atoms of this kind join together to form a bulk material the d-band is filled by this electrons. The different number of spin-up and spin-down electrons coming from each atom results in an asymmetric filling of the two spin sub-bands in the resulting metal. In Fig.2.3 is shown

the configuration of the two spin-bands: they are shifted in energy. This shift in energy is the result of the exchange interaction between electrons spin and the internal exchange field $\boldsymbol{H}_{ex}$. The 3d-electrons with the magnetic moments aligned with the total magnetization $\boldsymbol{M}$ inside the ferromagnet populate the sub-band with lower energy states, the ones with magnetic moments anti-aligned to the magnetization populate the sub-band with higher energy states (according to the interaction energy expression U=-μ.$\boldsymbol{H}_{ex}$). The net magnetization is in turn generated by this asymmetry in the number of spin-up and spin-down electrons. Due to the higher number of spin-down electrons (that in this case have magnetic moments aligned with the magnetization) present in the metal with respect to the spin-up electrons, a net magnetization in the spin-down electrons magnetic moment direction is obtained. On the contrary, the s-bands are much less affected by the exchange field, but they interact as well with the d-electrons. In the bulk material, the conduction-electrons wave function has contributions from s-like states as well as d-like states, resulting in a s-d hybridization. This means that the conduction properties of a ferromagnetic metal are linked to the s-electrons as well as the d-electrons.

The spin-down electrons are called *majority electrons* and they populate the *majority band*. On the other hand, the spin-up electrons are called *minority electrons* and they populate the *minority band*. The two types of electrons have a different conductivity. An expression for the conductivity for the two spin-channels is[17]:

$$\sigma^{\downarrow,\uparrow} = 1/\rho^{\downarrow,\uparrow} = \frac{e^2\tau^{\downarrow,\uparrow}D^{\downarrow,\uparrow}}{m^*}, \tag{2.13}$$

where $\downarrow$ and $\uparrow$ indicate spin-down and spin-up channel respectively, τ is the spin-relaxation time, D is the D.O.S. and m^* is the effective mass of electrons. So, according to a two-channels model for the electrical conduction[23], a ferromagnetic metal can be interpreted as made by two half-metals (an half-metal is an ideal metal where the electrical conduction is due to electrons with only one spin-polarization) in parallel. In this model, considering also the possibility that electrons from one channel can be scattered into the other one and vice versa, the resulting total resistivity is given by[17, 23]

$$\rho = \frac{\rho^{\downarrow}\rho^{\uparrow} + \rho^{\downarrow\uparrow}(\rho^{\downarrow} + \rho^{\uparrow})}{\rho^{\downarrow} + \rho^{\uparrow} + 4\rho^{\downarrow\uparrow}}, \tag{2.14}$$

where $\rho^{\downarrow\uparrow}$ is the spin-flip scattering resistivity contribution. From (2.14) is easy to see that if $\rho^{\downarrow\uparrow} << \rho^{\downarrow}$, $\rho^{\uparrow}$ the equation is redused to the resistivity expression of a perfect two-channels model

$$\rho = \frac{\rho^{\downarrow}\rho^{\uparrow}}{\rho^{\downarrow} + \rho^{\uparrow}}. \tag{2.15}$$

The resistivities of the two spin-channels are usually different. The probability of s-d scattering is function of the number of available energy states in the d-band at the Fermi level E_F. More available states means higher probability for the s-electrons to be scattered in the d-band, where the effective mass is higher and the conductivity is lower, according to (2.13). On the other hand, the DOS at the Fermi level is also different for the two channels. This means that the contributions ($I_{\downarrow}$and $I_{\uparrow}$) given to the total electrical current I_{tot}=$I_{\downarrow}$+ $I_{\uparrow}$ by the two channels are actually different. Dividing the spin-current I_{dif}=$I_{\downarrow}$- $I_{\uparrow}$ by the total current it is possible to define the *polarization* P

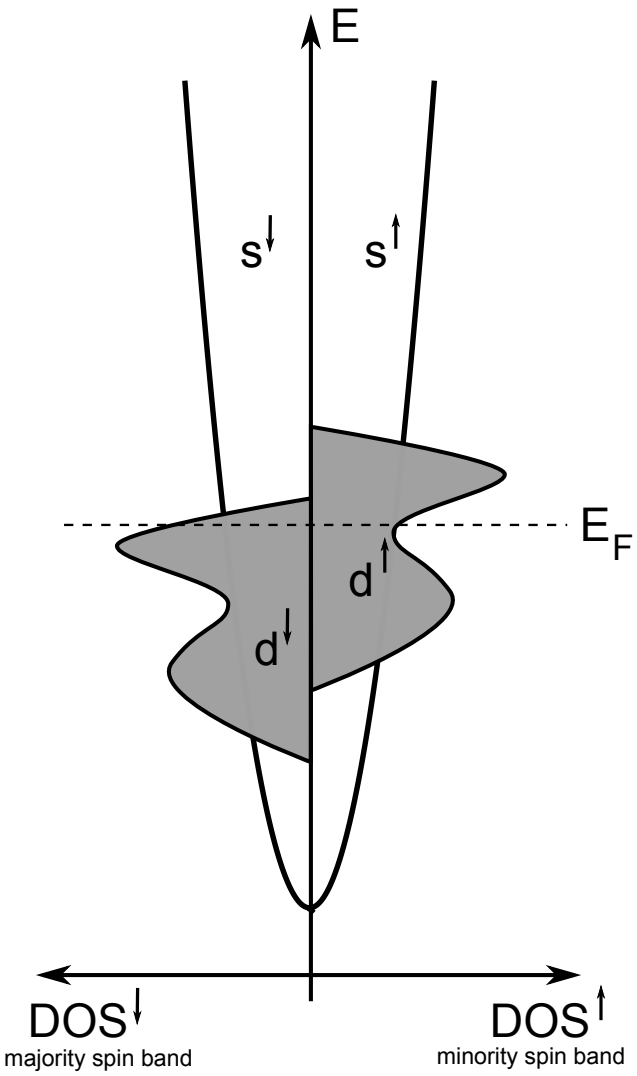

Figure 2.3: *Schematic of the DOS for a 3d-ferromagnet.*

of a ferromagnet[17]:

$$P = \frac{I_{dif}}{I_{tot}} = \frac{\sigma^{\downarrow} - \sigma^{\uparrow}}{\sigma^{\downarrow} + \sigma^{\uparrow}}. \tag{2.16}$$

According to the definition of the polarization of a ferromagnet, it is possible to speak about *majority* or *minority ferromagnet* when P>0 or P<0 respectively. In the first case the electrical conduction is mainly due to the majority electrons, in the second case it is due to the minority electrons. The polarization is a typical characteristic of each ferromagnetic material. For example, Fe is a majority ferromagnet (P$\simeq$ 40%); on the other hand, $Fe_{70}Cr_{30}$ is a minority ferromagnet (the one used by us in our experiments, it has a polarization P$\simeq -30\%$)[23, 24].

2.3 Metallic spin-flip based laser theory

2.3.1 Hot electrons as photons source

As stated in the previous section, in order to obtain the desired lasing effect the possibility of hot electrons injection in point contacts is exploited. Indeed, in this way it is possible to produce a spin-population inversion in the core of magnetic PCs. A theoretical description of this phenomenon is given in the article by Kadigrobov et al.[5], where the theory is presented for a single heterocontact made by a ferromagnet on one side and a normal metal on the other side, working in the diffusive regime. Applying an external magnetic field, the two conduction spin sub-bands in the normal metal are split in energy according to the Zeeman effect. Electrons with magnetic moment parallel (spin anti-parallel) to the magnetic field are pushed towards lower energy states, while the ones with magnetic moment anti-parallel (spin parallel) to the external field go towards higher energy states, according to the interaction energy expression U=-$\boldsymbol{\mu}$.$\boldsymbol{B}$. This situation is similar to the two-levels system, with a ground state and an excited state: if you have a mechanism which makes possible to pump electrons in the upper level it is possible to reach a condition where there are more electrons in the excited state (metastable state) than in the ground state. When these electrons decay towards the lower level, one of the possible channels of dis-excitation is the emission of photons. In our case the electrons could decay from the upper band to the lower band, emitting photons. This is the main physical idea of this project: to obtain a laser based on light production by spin-flip decaying of electrons between two separated spin-energy levels. An electron in the upper sub-band decays into the lower sub-band, the lost energy is converted into a photon and the total spin is conserved ($E_i - E_f = \hbar\omega$ and $S_i = S_f + S_{ph}$, where S_{ph} is the spin of the photon).

A necessary condition to make the laser work is to produce a population inversion into the active material. In this case it means to pump hot electrons from the ferromagnet to the normal metal (which is the active material here), in order to overpopulate the upper band. This can be obtained for example[5] applying a voltage to a point contact where the magnetization **M** in the ferromagnet is anti-parallel with respect to the applied external magnetic field **H** (Fig.2.4). Injecting electrons from the ferromagnet to the normal metal the two spin-currents have different probabilities to reach the normal metal. Thinking of using a "majority injector" (that is a ferromagnet where the electrical current is mainly due to the electrons with magnetic moments aligned with the total magnetization, the so called *majority electrons*), the majority electrons give a bigger contribution to the flowing current, so that a net spin-polarized current is injected into the normal metal giving us a spin

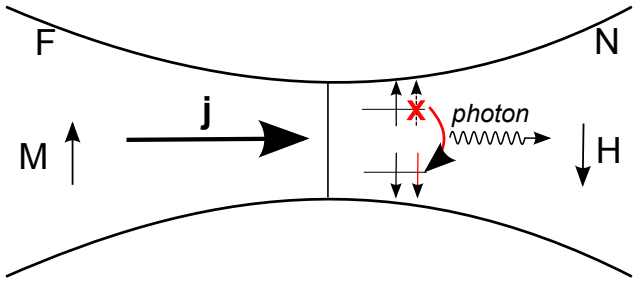

Figure 2.4: *Hot electrons injection from a majority ferromagnet injector to a normal metal with Zeeman-split conduction band in a diffusive point contact, with consequent photon emission. The small arrows represents the magnetic moments of electrons.*

accumulation. More precisely, with the geometry of Fig.2.4 the upper sub-band is overpopulated, and a spin-population inversion is obtained.

A theoretical description of the spin accumulation into the active material is given by Kadigrobov et al.[5]. Solving the Boltzmann equation for both the metals of the point contact they obtain an approximate expression for the electron distribution function $f_p^\sigma(\epsilon)$ into the normal metal:

$$f_p^\sigma(\epsilon) = \alpha_p^\sigma n_F(E_\sigma(p) + e\phi_0(r) - {}^{eV}/_2) + (1 - \alpha_p^\sigma) n_F(E_\sigma(p) + e\phi_0(r) + {}^{eV}/_2), \tag{2.17}$$

where σ indicate the two different spin projections (+1 for spin-down and -1 for spin-up electrons), α_p^σ is the probability an electron coming from the ferromagnet diffuses into the normal metal reaching the point $\boldsymbol{r}$ with momentum $\boldsymbol{p}$, n_F is the Fermi distribution function into the metal, $E_\sigma(\boldsymbol{p})$ is the electron energy without any bias (that is $E_\sigma(\boldsymbol{p})=\epsilon(\boldsymbol{p})+\sigma\mu_B H$ into the normal metal, with $\epsilon(\boldsymbol{p})$ being the electron energy without any field) and $\phi_0(\boldsymbol{r})$ is the electrical potential. A sketch of $f_p^\sigma(\epsilon)$ at zero-temperature is given in Fig.2.5.

By integrating $f_p^\sigma(\epsilon)$ over all the energy states we obtain two different densities for the spin-down and the spin-up electrons for a particular point $\boldsymbol{r}$ into the active volume, and this spin accumulation comes out to be dependent on the bias voltage [5]:

$$n_\uparrow(r) - n_\downarrow(r) \propto [(\alpha_\uparrow - \alpha_\downarrow)eV - 2\mu_B H]. \tag{2.18}$$

Then, integrating also over the active volume a final expression for the total spin accumulation can be obtained. So, it is clear that in order to activate a photons emission a threshold voltage has to be reached at the two ends of the PC.

Looking now at the band structure of the active material, the main feature is the Zeeman-splitting (or Exchange-splitting, in the case where also the active material is a ferromagnet) between the two sub-bands (Fig.2.6). Without a bias voltage the system is at the thermal equilibrium, and the Fermi level is constant everywhere in the point contact. Applying a voltage V the system goes in disequilibrium and a spin-polarized current starts to be injected into the active material. The upper band is filled by hot electrons with magnetic moment "up" (according to Fig.2.6) in a larger amount with respect to the lower band, and for "charge neutrality" into the metal a same amount of moment-up and moment-down electrons are removed. This gives a filling up of the upper band levels and an emptying of the lower band levels (Fig.2.6, red areas), resulting in the spin accumulation

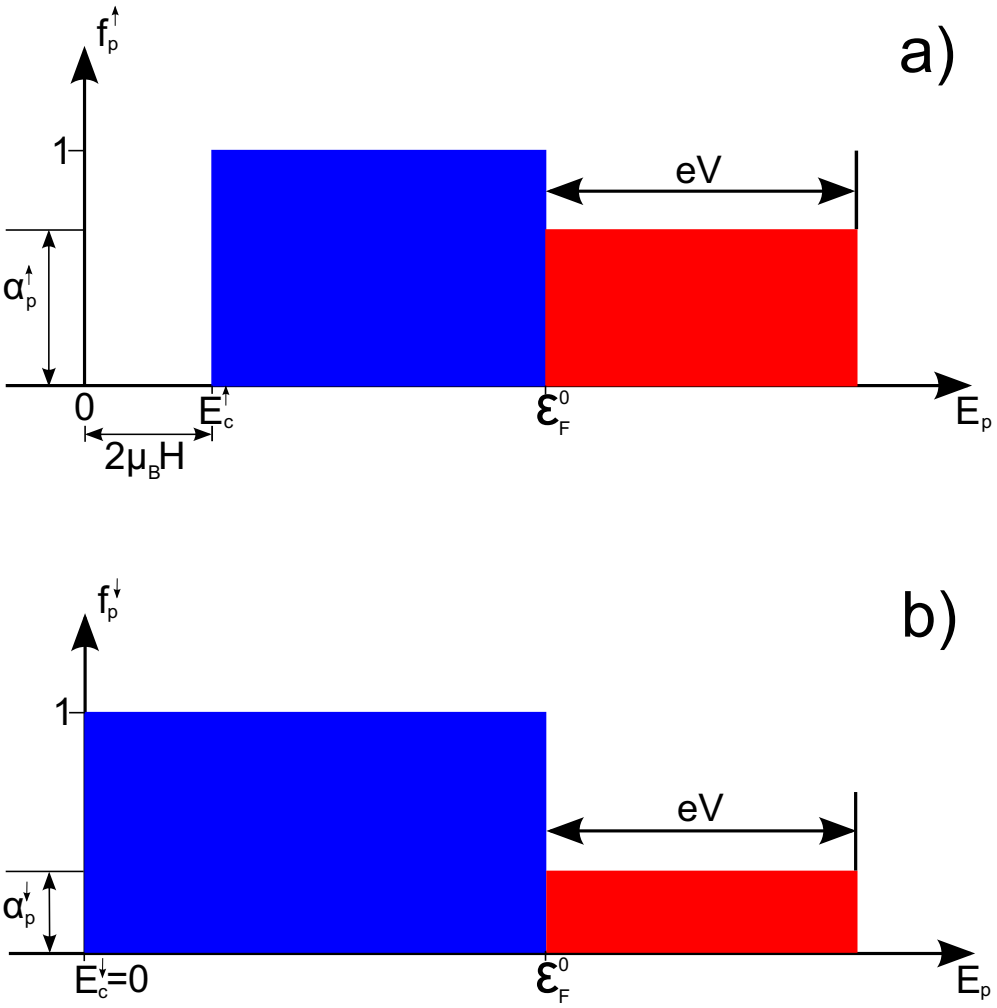

Figure 2.5: *Energy distribution functions at zero-temperature for a) spin-down (moment-up ↑) and b) spin-up (moment-down ↓) electrons in the active material at the point* $\boldsymbol{r}$*. The bottom of the conduction sub-band for ↓-electrons* $E_c^{\downarrow}$ *is taken as zero-energy level, so that* $E_c^{\uparrow} = 2\mu_B H$*, the Zeeman-splitting. The blue areas describe the zero-bias situation, where all the electron-states up to the Fermi level* E_F^0 *are filled in both the sub-bands. When a voltage* V *is applied to the PC, hot electrons are injected into the active material, with different probabilities* $\alpha^{\uparrow}$ *and* $\alpha^{\downarrow}$*, for moment-up and moment-down electrons respectively. At a particular voltage value* V_{th} *the spin-down density overcomes the spin-up density, and the spin population into the normal metal is inverted, so that* $n_{\uparrow} > n_{\downarrow}$ *if* $\alpha_{\uparrow} > \alpha_{\downarrow}$ *(see text for details). Figure from Kadigrobov et al.[5].*

above. When an opportune threshold voltage will be reached, vertical transitions ($\boldsymbol{k}_i$=$\boldsymbol{k}_f$) for excited electrons will be possible and photons emission will start.

Kadigrobov et al. not only gave a theoretical description of the possibility of photons emission in a magnetic point contact, but they demonstrated it experimentally. They obtained absorption and emission of photons in a PC made by a magnetic layer (FeCr) in contact with a normal metal needle (Cu), with an external DC magnetic field and a resonant e.m.-radiation applied[5]. The emission of light has been detected as an increase in the PC-resistance value, when the applied magnetic field H was in resonance with the radiation. According to them, this is a demonstration that light emission actually happened. By emitting light the system dissipates energy, and electrically this is like an increase in the total resistance.

Different combinations of magnetic materials, magnetic field directions and bias-voltage sign are possible for obtaining photons emission. In the case of majority injectors, it is possible to generate a spin-population inversion in two different ways[6]. With a magnetic field $\boldsymbol{H}$ anti-parallel with respect to the magnetization $\boldsymbol{M}$, applying an opportune voltage V so that it injects electrons into the normal metal we can obtaine spin accumulation and conseguently light emission as described above. On the other hand, it is possible also to work with a magnetic field parallel to the magnetization. In this case the excited electrons into the normal metal are minority electrons into the magnetic material. In order to produce a spin population inversion it is necessary to apply a voltage with opposite sign with respect to the previous case. In this way majority electrons (that is, the electrons which populate the lower energy states into the active material) are more easily removed from the normal metal, due to their bigger mobility into the ferromagnet and to the reflection of the minority electrons at the F/N interface (see Fig.2.7). It is possible to use also a minority injector in order to produce photons emission by PCs. In this case the magnetic field has to be parallel with respect to $\boldsymbol{M}$, so that the excited electrons into the normal metal are the minority electrons into the ferromagnet. Due to their higher mobility, the minority electrons are injected, by a voltage V, into the normal metal. Again a spin population inversion is generated and the lasing effect becomes possible (as in the case of FeCr/Cu PCs used in [5]).

2.3.2 A spin-flip based laser proposal

Due to the evidence of photons emission by a single magnetic point contact[5, 6], it becomes possible to propose a laser based on it. A sub-wavelength therahertz spin-flip laser based on a PCs-array was proposed by Shekhter et al.[7]. The main idea is to increase the optical power by connecting in parallel many point contacts. Such idea will be the key for the future laser (Fig.2.8).

By creating an array of nanometric apertures ($d \simeq 10-20$ nm) into an insulating layer 10-15 nm thick, it is possible to patter an array of magnetic PCs. Indeed, if a magnetic layer is covered by this dielectric mask and then a non-magnetic metal is used to fill in the apertures, an array of magnetic point contacts in parallel is obtained. Finally, two electrodes at the two ends of the structure give us a laser with a cylindrical resonator. All the structure is disk-shaped, the two electrodes confine the light in the vertical direction and the step in the refractive index at the dielectric/air interface confines the light into the plane. This open-resonator geometry choice is supported also by the experimental observations done by Monakhov et al.[8] on their semiconductor sector-disk lasers. "Whispering gallery modes" have been theoretically demonstrated and then experimentally observed for full, half and quarter-disk lasers.

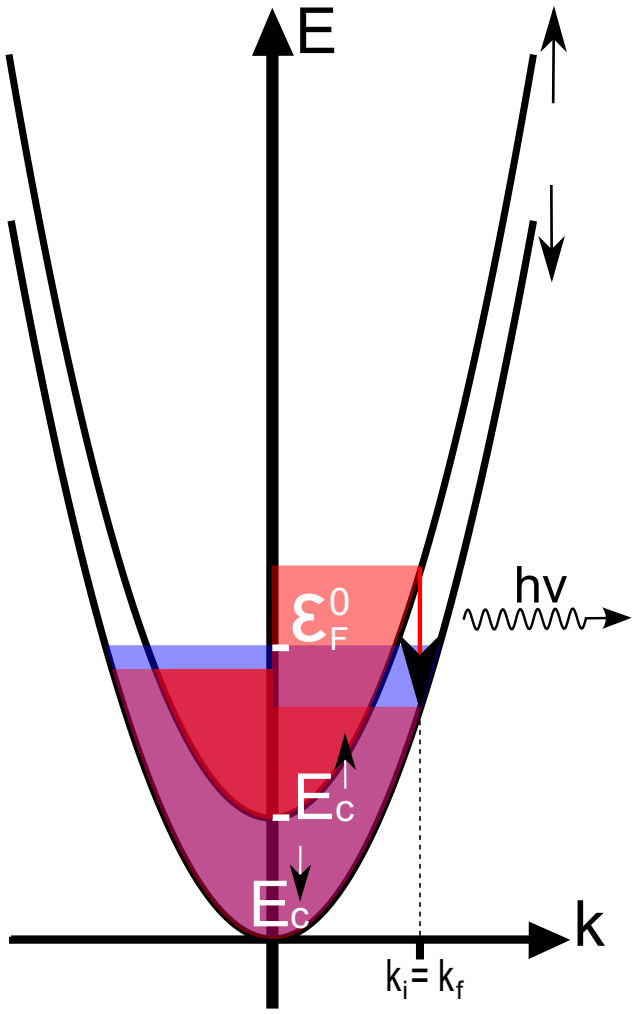

Figure 2.6: *Simplified conduction band structure for the normal metal with an applied magnetic field. The blue areas describe the zero-bias situation, where all the electron-states up to the Fermi level E_F^0 are filled in both the sub-bands. When a voltage V is applied, a disequilibrium is generated into the energy states occupation. ↑-electrons and ↓-electrons are injected into the normal metal with different probabilities, resulting into a spin population inversion (red areas). At a particular threshold voltage V_{th}, vertical transitions with subsequent photons emission occur between the two sub-bands, according with the total spin conservation law.*

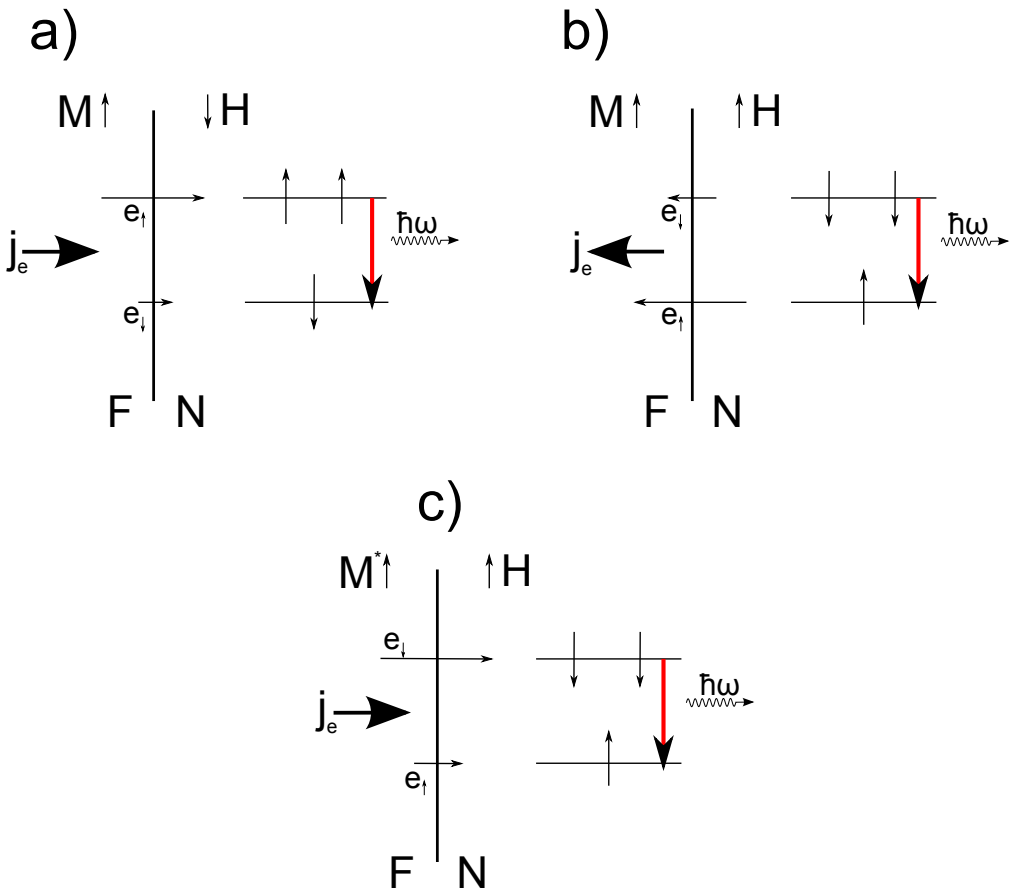

Figure 2.7: *Three different set-up for obtaining photons emission from a magnetic point contact. In a) and b) the ferromagnet (F) is majority-type. In the first case the magnetic field is applied anti-parallel to M, so that a flux of electrons from F to N is needed to produce a spin-population inversion in the normal metal (N, active material). In the second case H is parallel to M, and a flux of electrons from N to F gives us the desired population inversion. On the other hand, using a minority injector (M^*), in order to produce a spin-population inversion into N a flux of electrons from F to N and H parallel with respect to M^* are needed. After Naidyuk et al.[6].*

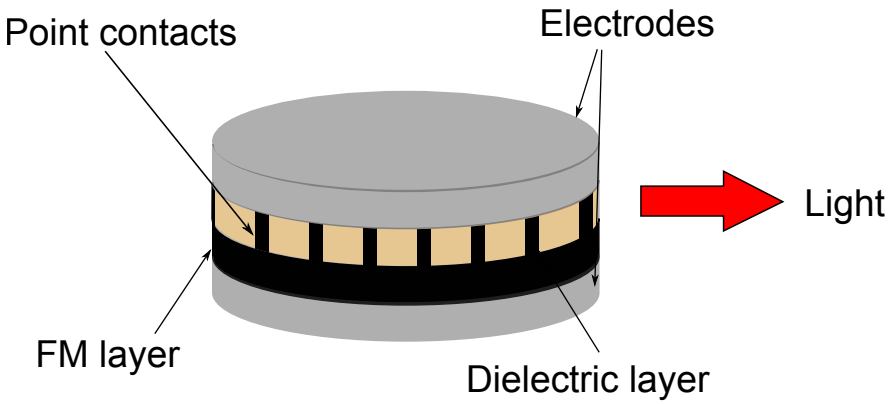

Figure 2.8: *Schematic of a proposed sub-wavelength disk laser by Shekhter et al.[7]. The cylindrical resonator confines the light by the two metallic electrodes in the vertical direction and by the refractive index step at the dielectric/air interface in the disk plane. Light can be detected by the lateral edge of the resonator.*

In the work by Shekhter et al.[7] the lasing modes have been studied by solving a lasing eigenvalue problem (LEP). Maxwell's equations are solved with respect to the boundary conditions given by the disk-shaped surface and the radiation at infinity. In this way coupled values for the lasing frequency and the threshold optical gain are obtained. While the working λ is selected by tuning the magnetic field around the frequency value we would like to obtaine[2] ($\hbar\omega = 2\mu_B H$), the effective lasing mode m is determined by the resonator diameter $2a$ ($2\pi a \simeq m\lambda$, for full-disk as well as half-disk resonator).

The feature that makes this metallic PCs-based spin-laser interesting is the high electrical current density that can be reached in PCs. The possibility to inject ultrahigh electrical current densities into the PCs ($J \sim 10^9 \mathrm{A/cm^2}$[6, 7]) makes possible to reach very high levels for the optical gain ($g_{PC} \sim 10 - 100$ cm^{-1}, much higher if compared to the one obtained in semiconductor disk-lasers, g=27 cm^{-1}, [7]), due to the high spin-population inversion which would be obtained.

[2] In the case of poin contacts obtained at the interface between two ferromagnetic materials, is the exchange-splitting into the ferromagnet which acts as active material that fixes the frequency of the radiation.

Chapter 3

Experimental instrumentation

In this chapter is given a brief overview of the main instruments used for the device fabrication. The entire process (see Ch. 4) for samples patterning is quite complex, and several tools have been used: a sputtering machine and an electron beam evaporation (EBE) system for thin films deposition; a photo-lithography machine and a colloidal lithography technique for sample patterning; ion milling as well as reactive ion etching (RIE) systems for patterning transfer.

3.1 Magnetron sputtering system

One of the most used techniques for metallic or insulator thin film growth is the sputtering. Such technique gives us films with low roughness (a few nanometers) and is quite compatible for industrial processes. It mainly consists in bombarding a material target by high-energy ions (usually Ar^+) and the erupted atoms from the target are deposited on a substrate.

For an high purity and quality of the films, it is fundamental to generate a high vacuum environment where the desired material is deposited. For this reason all the system is enclosed into a metallic chamber connected to a turbo pump. Generating of the vacuum ($\sim 10^{-5}$ mTorr, in our case) gives us two important effects: first, the concentration of contaminating particles (for example: O_2, H_2O, N_2 and CO_2) is strongly lowered into the chamber, so it is possible to depose layers of the material we desire with a low impurities contamination; secondly, working at very low pressure it is possible to control very well the thickness of the growing layer. Thinking of a gas closed in a chamber, the rate of deposition of the gas on a surface is given by [9]

$$N_i = \iota \frac{p}{\sqrt{2\pi m k_B T}}, \tag{3.1}$$

where p is the gas pressure, m is the mass of a gas molecule/atom, ι is the sticking coefficient (the probability that a molecule/atom which is impinging on the surface gets absorbed), k_B is Boltzmann's constant and T is the temperature of the gas. How it can be seen in (3.1), the rate of deposition of a material on a surface is directly proportional to the pressure of the gas: the higher the pressure, the higher the velocity of deposition. For example, at room temperature, with a pressure of 1 atm, a molecular mass of 20 u.m.a. (m=3.6x10^{-26}Kg) and a sticking coefficient equal to 1, the deposition rate is 3.27x10^{27}m^{-2}s^{-1} [9]. This means that in 1ns the deposition of a monolayer of

Figure 3.1: *AJA Orion Sputtering System in the Nano Fabrications Lab at the Applied Physics department at KTH.*

10^{18} molecules is obtained. This makes very difficult the control of the thickness of deposition. On the other hand, working at a pressure p=10^{-6}Pa ($\sim 8 \times 10^{-6}$mTorr) N_i becomes 3x10^{-16}m^{-2}s^{-1}. Now to depose one monolayer of the gas before we need about 30 seconds, so that it is much easier to control the thickness of the film on the nanometric scale.

For this work has been used a magnetron sputtering system: *AJA Orion Sputtering System*[1] shown in Fig. 3.1 and Fig. 3.2. The system has 8 magnetrons connected to DC and RF power supplies, and a rotating sample holder. The sample can be cleaned before deposition by an Ar-plasma. The structure of each magnetron sputtering gun into the system is sketched in Fig. 3.3. It consists of a target material embedded between two electrodes: a target electrode directly in touch with the target and a ground shield electrode in front of the target. Under the target are some magnets ($SmCo_5$) generating a magnetic field whose lines go across the target. When a gas is injected into the chamber (Ar in this system), the high electric field generated by the voltage between the two electrodes produces Ar-plasma on the target and accelerates Ar^+ ions towards the

[1] *ATC Orion Sputtering System, by AJA INTERNATIONAL, INC., North Scituate-MA (USA).*

Figure 3.2: *Main chamber of the AJA Orion Sputtering System. We can see the circular geometry in which the sputtering guns are positioned inside the chamber.*

target so that atoms are emitted from the surface of the target. The atoms flow which is generated is used to deposit thin films of the target-material on the surface of the sample. The magnetic field generated by the magnets helps to trap the ions on the target.

It is important to notice that during the deposition of a magnetic material the field generated by the magnets could have problems in crossing the target, due to the capacity of the ferromagnet to block field's lines. So, usually magnetic targets are thinner than normal-metal or dielectric targets. Also a different central magnet (Fe core) is used in order to make easier for field's lines the crossing of the target. While, in the case of dielectric targets the problem is their charging due to the trapping of Ar-ions. In order to avoid this situation, where the danger of electrical discharges on the target surface is real, an AC voltage rather than a DC voltage is applied.

3.2 Electron beam evaporation system

In an E-Beam Evaporation System a high energy electron-beam is focused on the material which we would like to deposit. Two different configurations are possible: a rod-feed system, where a rod is rounded by a filament (usually made of Tungsten) where a thermionic electrons emission is obtained by applying current to it. A high voltage bias between the rod and the filament accelerates the emitted electrons towards the rod, so that it gets hot and atoms start to evaporate away from it (Fig.3.4_b). An other configuration consists of a crucible containing the material to deposit and an electron beam still produced by thermionic emission from a filament. It is accelerated by an high voltage and at the same time focused on the crucible by a magnetic field (Fig. 3.4_a). In this case

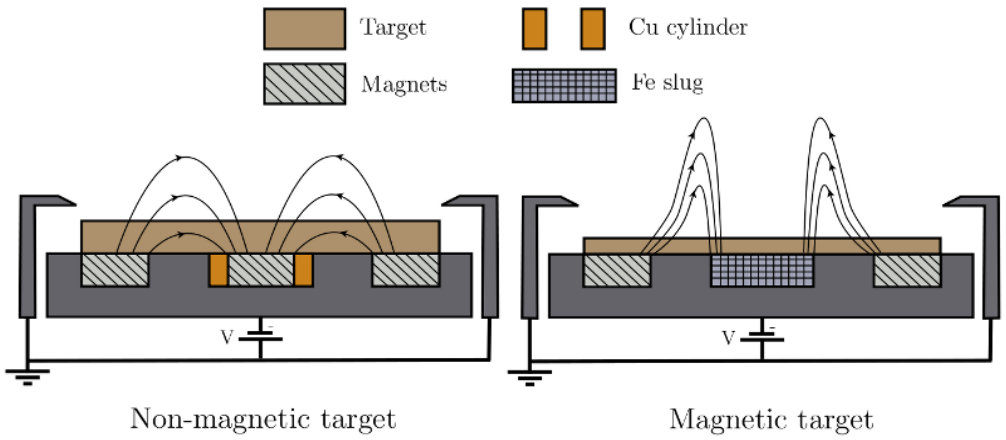

Figure 3.3: *Schematic of a sputtering gun in the AJA Orion System. On the left the configuration for non-magnetic targets is illustrated, where the target thickness is about 6 mm and the middle magnet is of the same kind of the peripheral ones. Field's lines across the target are shown. On the right the configuration for magnetic targets is reported. The thickness of the target is 3 mm and the middle magnet is substituted by an Fe core, so that even in this case it is possible for field's lines to cross the target. In both the images, the bottom (target-electrode) electrode and the ground shield enclose the target, and by the bias V a high electric field is produced on the target, making possible the plasma ignition.*

the material in the crucible starts to melt on the surface, where it is heated by the electron beam, and atoms starts to evaporate. In both systems a sample holder with the substrate is placed in front of the crucible/rod, so that the evaporating material can be deposited. Obviously, these kind of systems work in high vacuum conditions, so all has been told in the previous section about the necessity of generating an high vacuum environment still holds.

During this work have been used three different kind of e-beam evaporation systems. A rod-feed e-gun deposition system called "Sputnik" has been used for Aluminium deposition and Argon-ion milling (Fig. 3.5). In the Sputnik was possible to deposit material at a vacuum of 10^{-7} mbar ($\sim 7 \times 10^{-5}$ mTorr), while a vacuum of 10^{-9} mBar can be reached by the large turbo pump at non-deposition condition.

On the other hand, two different e-beam evaporation systems with crucibles have been used for thin films depositions during the sample-fabrication process: the Eurovac UHV E-Beam Evaporation System and the Edwards HV E-gun Evaporation System (Fig.3.6). In the Eurovac system it was possible to evaporate 5 different materials: Cr, Ti, CoFe, Au and Ge. The deposition pressure was usually around 10^{-4}mbar. For this project it has been used for thin films evaporation of Au and Cr (see next chapter). The Edwards system has been used mainly for Al_2O_3 and Al deposition. The common deposition pressure was about 2-3x10^{-5} mbar. In these systems, the thickness and the rate of deposition is controlled by a *SQM-160 Rate/Thickness Monitor* by *Sigma Instruments*. A gold plated quartz crystal in the chamber change its oscillation frequency with respect to its thickness, so that when material is deposited on it the resonance frequency of the crystal changes. Monitoring the resonance frequency it is possible to calculate the rate of deposition, and by a time-integration also the thickness of the deposited film. The resolutions are about 0.06Å/s and 0.027Å for the

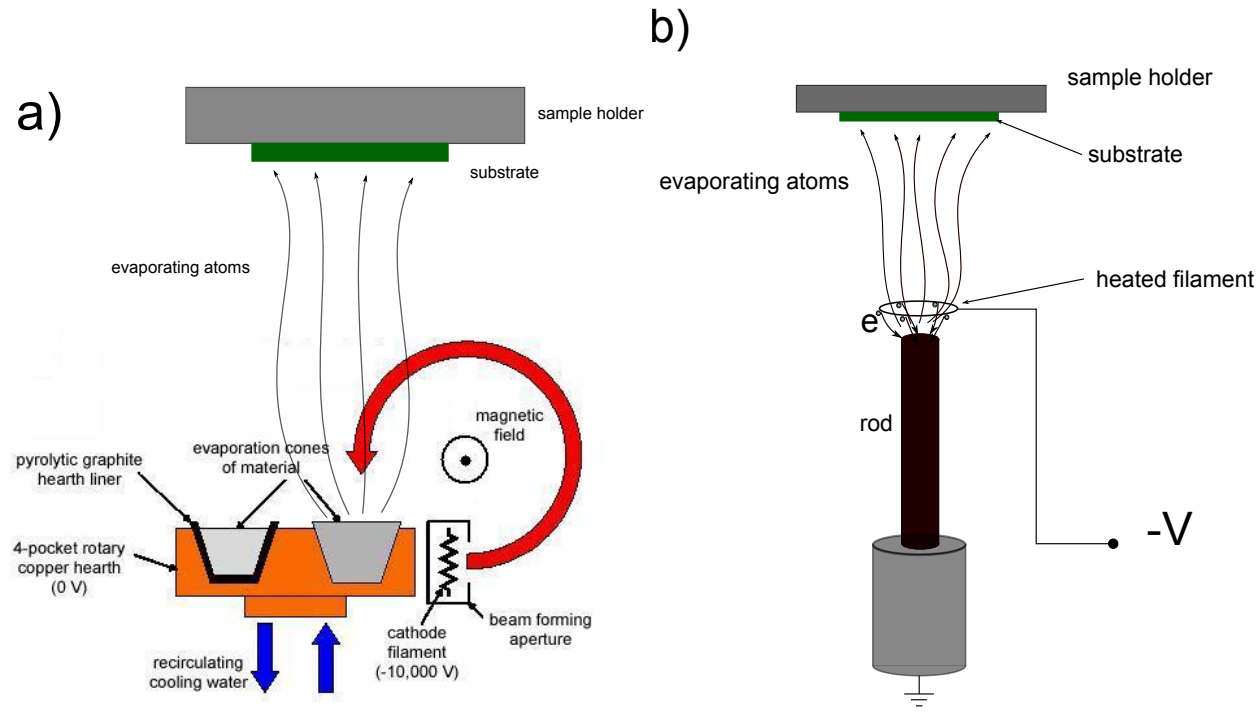

Figure 3.4: *Schematic of the two different e-beam evaporation systems used for this work. On the left a crucible contains the material to evaporate, while a thermionic e-beam is accelerated by electric field and focused by a magnetic field on the top of the crucible. On the right the typical configuration for a rod-feed e-gun system, where a rod made of the material to evaporate is heated by an accelerated thermionic e-beam and the evaporating atoms deposit on the surface of the substrate.*

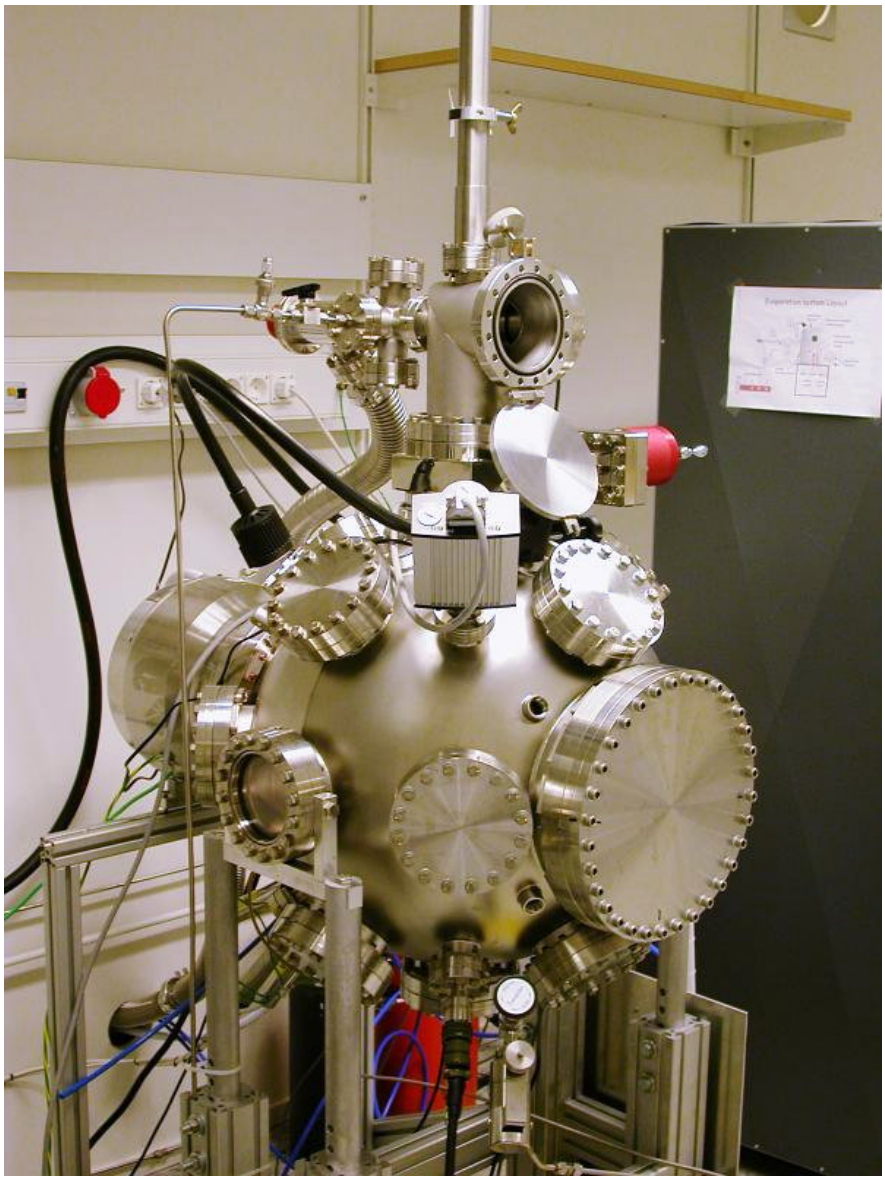

Figure 3.5: *The rod-feed e-gun deposition/Ar-ion milling system "Sputnik" in the Nano Fabrications Lab at the Applied Physics department at KTH.*

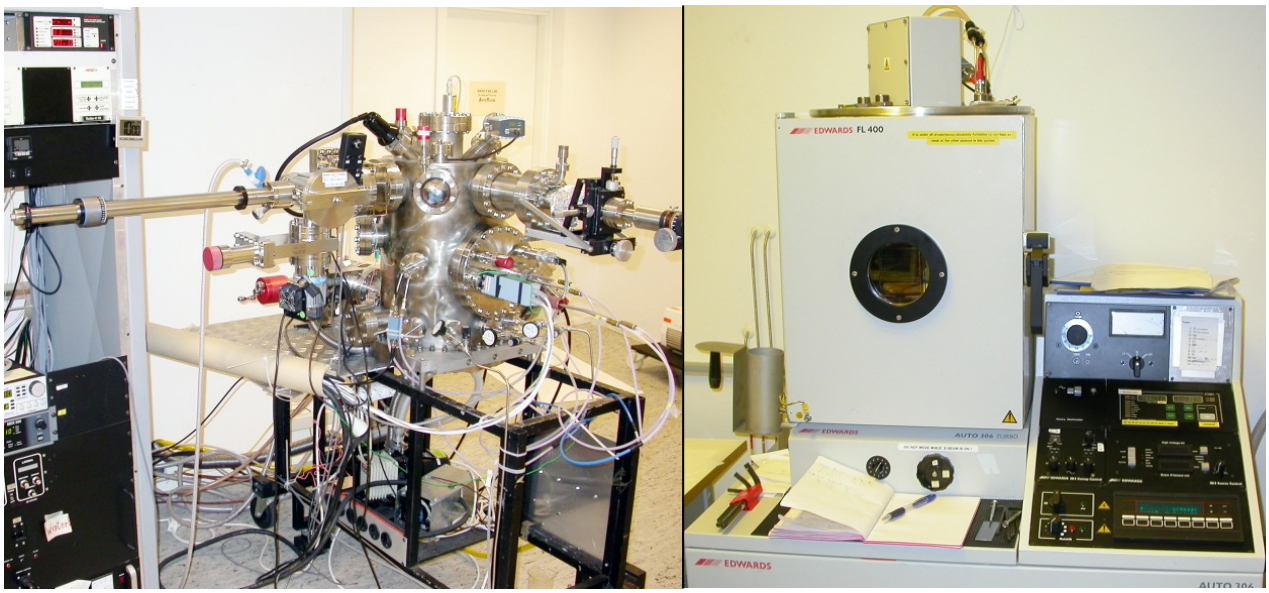

Figure 3.6: *The two electron beam evaporation systems with material contained into crucibles in the Nano Fabrications Lab at the Applied Physics department at KTH. The Eurovac UHV E-Beam Evaporation System on the leftt and the Edwards HV E-gun Evaporation System on the right.*

deposition-rate and the film thickness respectively (by specifications).

3.3 Optical Lithography

In order to pattern the sample the photo-lithography technique has been used. The maschine used is a *"Karl Suss MJB3" Mask Aligner* (Fig. 3.7), which works in contact mode and have a vacuum system for blocking the mask on the mask-holder. The light source is a Hg Arc Lamp with its three main UV lines (i-line at 365 nm, h-line at 405 nm, g-line at 436 nm). Electrical discharges excite Hg vapor, and when an excited electron comes back to the ground-state in a Hg-atom a photon mostly with one of these three typical wavelengths is emitted. The produced light is driven on the sample by an optical system (Fig. 3.8 [10]).

In the three different lithography steps of the sample-patternig process both positive and negative resists have been used. In each step a two-resists technique was exploited in order to obtain an undercut (see Fig.3.10 in the next paragraph). The reasons why an undercut is desired will be clear in the next chapter, where the sample-fabrication process will be exposed and discussed in details. The principle in the optical lithography is simple: the sample is first of all covered by a polymeric solution sensitive to the light (photo-resist), then it is illuminated via a metallic mask placed on it, so that only the uncovered parts of the sample are actually exposed to the light. According to the type of photo-resist, in the exposed areas the chemical bonds in polymeric chains are broken (for polymers like PMMA=Polymethil-methacrylate) or built (like in the case of HSQ=Hydrogen silsesquioxane) for a positive or negative photo-resist respectively. Finally, by an appropriate developer, the parts of the resists with shorter polymeric chains are removed from the sample surface. At this point

Figure 3.7: *Kars Suss MJB3 Mask Aligner in the Nano Fabrications Lab at the Applied Physics department at KTH.*

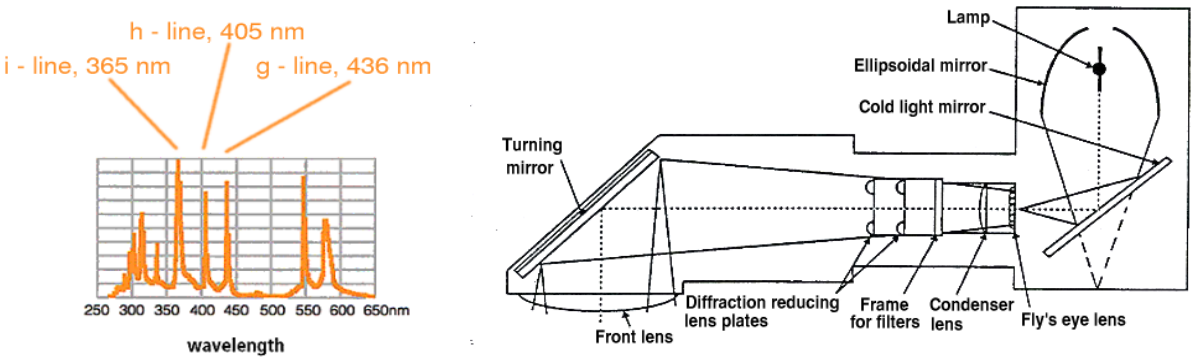

Figure 3.8: *On the left, the typical spectrum of an Hg Arc Lamp is reported, with its three main emission lines in the ultra-violet range. On the right, a schematic of the optical system used in the photo-lithography machine for positioning the light on the mask-sample system.[10]*

the sample is ready for the patterning-step, that can be made by ion-milling or by an evaporation process. At the end, the residual resist is removed by a remover (lift-off process) and the desired pattern is obtained.

The deposition of an homogeneous layer of photo-resist on the surface of the sample is done by a spin-coater (Fig.3.9). After that a few drops of the photo-resist are droped on the sample, the holder on which the sample is attached (by vacuum technique for example) is spun at high speed (1500-8000 rpm). It results that the thickness of the resist-layer depends on the spin-speed as well as on the viscosity and the concentration of the polymeric solution. An empirical expression for the thickness of the resist t is

$$t = K\frac{C^{\alpha}\eta^{\beta}}{\omega^{\gamma}}, \tag{3.2}$$

where K, α, β and γ are calibration constants, C is the concentration of the polymer, η is the viscosity of the solution and ω is the rotational speed. Before the exposure process the resist is baked for a certain amount of time which can varies from process to process. The tickness of the final layer can range between 0.5-2 μm.

3.4 Etching techniques

In the patterning process of the device two different etching techniques have been used: Ar-ion milling and Reactive Ion Etching (RIE). The Ar-ion milling process was obtained in the Sputnik system (Fig.3.5). A localized plasma is generated near the Ar-gun, so that in the plasma there are Ar atoms, Ar^+ ions and electrons. Plasma is created by an electric field wich accelerates electrons (usually generated by an hot W-filament by thermionic emission). Accelerating electrons hit molecules of the noble gas and ionize them. By a third electrode Ar^+ ions are accelerated normally towards the sample surface. After a neutralization of the positive ions by a second electrons source, the flux of Ar atoms hit the sample surface and knock of atoms from the sample, after bond breakage, by

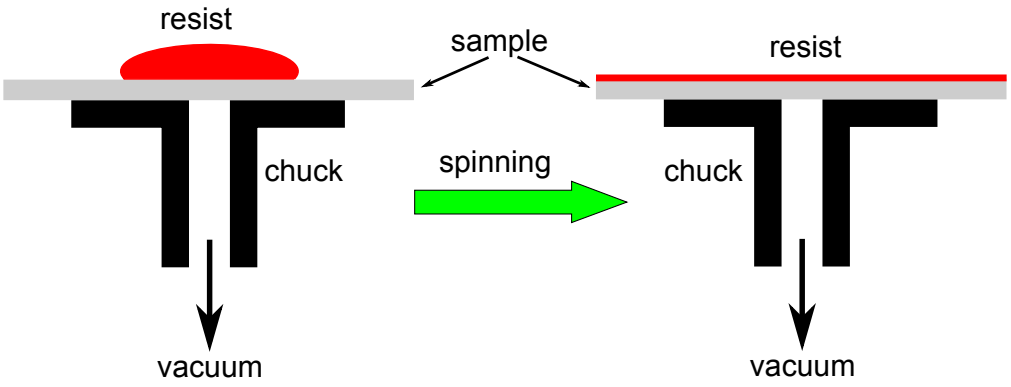

Figure 3.9: *Sketch of the spin-coating process for dispensing photo-resist on the sample surface. The situation before (left) and after (right) the spinning of the resist are shown.*

momentum transfer. Ar atoms are chemically inert, so that the interaction with the sample is only physical and the resulting etching is anisotropic (Fig.3.10).

For the Reactive Ion Etching process a *"Plasmalab System 100" by Oxford Instruments* have been used (Fig.3.11). In this system was possible to execute etching with the following gases: O_2, Ar, CF_4, CHF_3, SF_6 and Cl_2. For this work only O_2, Ar and CF_4 have been used in the several etching processes (see next chapter). Like in the ion milling process a plasma is generated in RIE technique as well. An RF plasma is generated into the chamber by an RF voltage between two electrodes placed one below and one above the sample holder and consist of (in the case of CF_4): electrons, CF_3^+ ions and F radicals (Fig.3.10). In this case two different etching processes can happen: a chemical etching, where radicals F chemically react with the sample material, giving an isotropic etching (and resulting undercut); a physical etching due to the acceleration of ions towards the sample (due to the charging of the sample by impinging electrons, for example), so that an anisotropic component perpendicular to the sample surface is added. The latter etching process helps also the radicals to penetrate, so that the etching rate is increased. The degree of anisotropy is toned by balancing the two etching components: the physical sputtering process and the chemical etching process. In addition, in the Plasmalab System 100 it is possible to produce an Inductive Coupled Plasma-ICP. An RF coil placed orizontally above the sample increases the ions concentration close to the sample surface, without adding kinetic energy to them. In this way the etching rate is increased. This technique results fundamental for the success of the isotropic nanoparticles etching process needed in this work (see next chapter for details).

Finally, it is important to state that if the ion milling technique is non-selective with respect to the material of the sample, on the other hand the RIE is much more selective. This is why for etching processes on all the sample area, where all the materials presented on the sample surface have to be etched without any distinction is made by ion milling process; while etching processes where it is desired to attack only one kind of material are made by chemical etching. It is important to clarify also that, even if the ion milling process has almost no selectivity with respect to the material, it is also true that the etching rate for metals (Al, Cu, Au and Fe in our case) is usually ten times higher than for insulators (SiO_2 and Al_2O_3) according to our measurements.

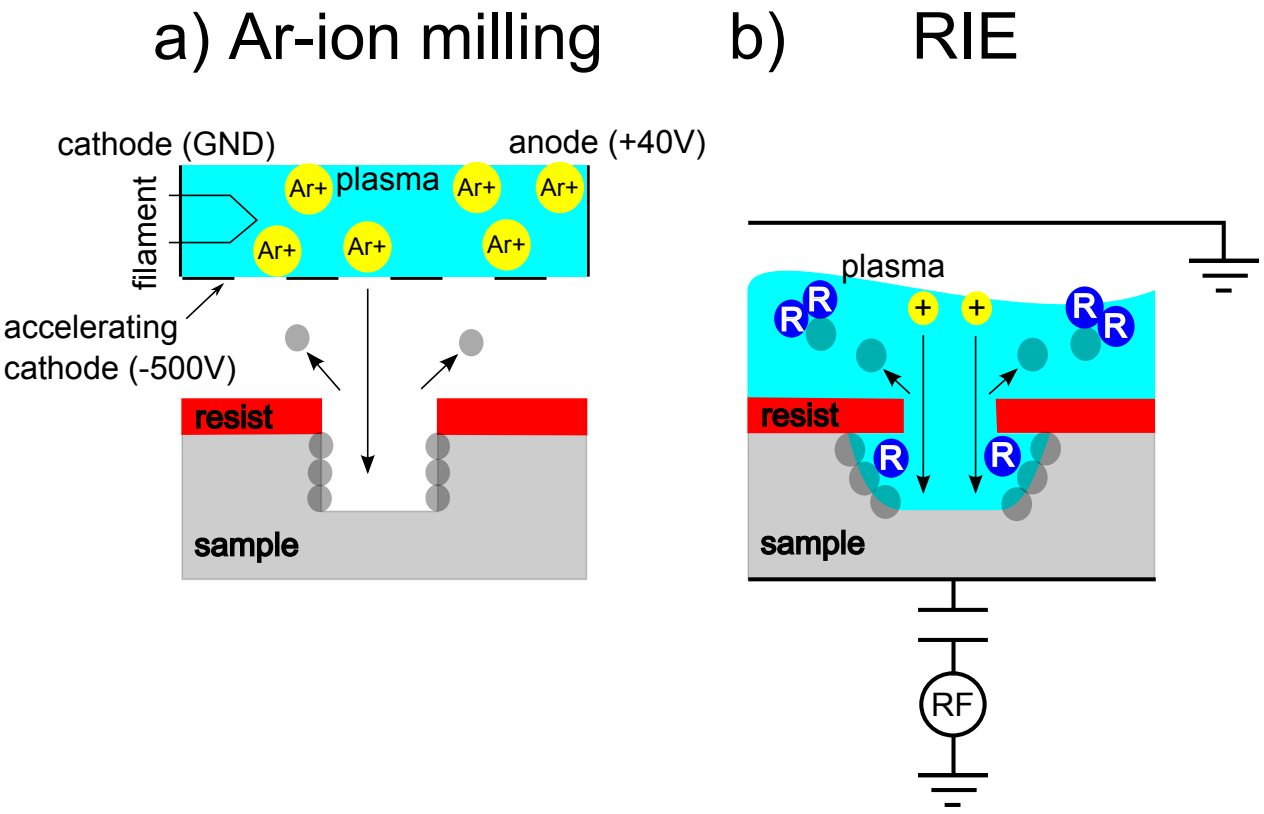

Figure 3.10: *Schematics of the Ar-ion milling technique and the Reactive Ion Etching technique. In a) an Ar-ions beam is accelerated from the plasma towards the sample surface, where sample atoms are sputtered away from the sample. This is a pure physical etching process and no undercut is obtained. In b) the positive ions into the plasma are accelerated towards the sample, where they produce a milling process, but at the same time the radicals (R) interact chemically with sample's surface, so that atoms are removed isotropically and undercut can be obtained . This second process is a mix between physical and chemical etching, and the possibility to balance the power of the two processes makes possible to tune the degree of anisotropy of the etching.*

Figure 3.11: *Plasmalab System 100 RIE machine by Oxford Instruments in the Nano Fabrications Lab at the Applied Physics department at KTH.*

Chapter 4

Patterning process for device fabrication

The aim of this chapter is to give a complete description of the process done in the nano-fabrication lab at the Applied Physics department of KTH, in order to obtain the desired device. Several patterning processes has been used in order to fabricate the proposed spin-flip based laser. Different shapes for the resonator as well as for the entire chip have been tried, in order to obtain a device with the desired characteristics. After an initial full-disk-shaped device (see Fig.**??**, 5.5 in the chapter "Measurements technique and experimental results"), where the complite cylindrical structure was covered by a metallic coating (the top contact), an half-disk-shaped resonator has been preferred in order to make the detection of the light easier. Indeed, in this second configuration the flat lateral edge of the resonator is not covered by a metallic coating (see Fig.4.8), so the light emitted from that side has a higher intensity. The chosen configuration is based on the previous observation done by Monakhov et al.[8], where light has been detected from an half-disk semiconductor laser at the flat edge, and the power detected was higher than in the full-disk and quarter-disk configurations.

In this chapter will be exposed the entire process for the device fabrication, in the last configuration of half-disk resonator. Anyway, the process was the same also for the other configurations. The only difference was the different mask used in the photo-lithography steps. Along the process description there will be some discussions about the experimental results and/or difficulties encountered during the lab-work, in addition to a description of the technical features which characterize each step.

1. LITHOGRAPHY 1 (BOTTOM-CONTACTS PATTERNING): the starting structure is a multilayer [1] consisting of (the numbers in brackets indicate the thickness of each layer in nm) $Cr(2)/Al(150)/Cr(10)/SiO_2(15)$, deposited on a substrate made of 1μm of SiO_2 on a wafer of Si (structure sketched in Fig.4.1). Two different photo-resists are spin-coated on the top surface of this structure, so that the undercut technique can be exploited. In this bi-layer technique, first of all is spinned a layer of $LOR\text{-}7B$[2] (R1) at 5000 rpm (Rotations Per Minute) for 1 min, and then baked at 190^oC on a hot plate for 5 min. A layer of 500nm in thickness is obtained, as reported also in datasheets about this kind of resist (see for example [15]). A

[1] At the same time my advisor Dr. Adrian Iovan executed the same patterning process (with just few changings) with an initial Cu substrate.

[2] *MicroChem Corp.*, Newton, MA, U.S.

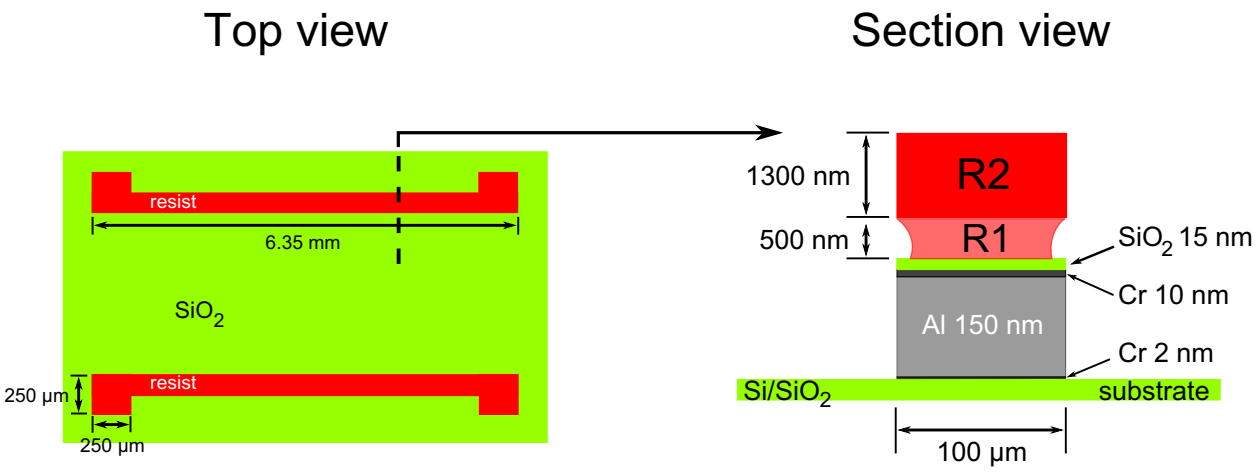

Figure 4.1: *Schematic of the patterning process for the bottom-contacts. The "Top view" shows the stripe-shaped bottom-contacts after the ion milling, covered by the double layer of resist on the top. On the right, a section of the patterned structure is shown, with all the metallic layers indicated. Note that the figure is not in scale and the sizes of the different parts are not in the same proportion of the real structure .*

second positive photo-resist, *Microposit S1813*[3] (R2) is spinned at 4000 rpm for 1 min and subsequently backed at 115^oC for 1 min. A layer of about 1300nm in thickness is obtained, as reported in datasheets about this kind of resist (see for example [16]). At this point a chromium mask is aligned by the mask aligner on the sample, which is exposed for 5.5 sec to UV radiation. Finally, is made a development process in the *Microposit MF-319 Developer*[4] for 25 sec. After checking at the optical microscope that no resist is still attached on the sample in the exposed areas and that the undercut is well defined, the sample is prepared for the patterning process by Ar-ion milling.

2. Ar-ION MILLING (BOTTOM-CONTACTS PATTERNING): 2 hours of Ar-ion milling are processed on the sample. After calibrations, it is known that this leads to the etching of all the metallic multilayer structure, so that the insulating SiO_2 substrate is reached. A 180nm are etched, giving the patterning of the bottom-contacts of the device (Fig.4.1). The etching parameters are: $7x10^{-5}$ mbar for the pressure into the etching chamber; 38.0 V is the discharge voltage for the plasma ignition; 350.0 V is the acceleration voltage (ion-beam acceleration voltage); 2.70 A is the cathode filament current for electrons emission.

3. RESIST REMOVAL: in order to remove the remaining resist from the sample surface, we use *Microposit Remover rem-1165*[5] into a beaker. The beaker is heated for 30min at 50^oC, so that the remover can better attack the residual resist. After the 30min, the sample is cleaned

[3] *Shipley Company*, Marlborough, MA, U.S.
[4] *DOW Chemical Company.*
[5] *Rohm and Haas Company*, Philadelphia, PA, U.S.

by Isopropanol and dried by an N_2-flux, and subsequently checked at the microscope to see if all the resist has been removed. In case of uncleaned sample, an ultrasound process is used at low power (in order to not damage the patterned structure) for 2min with the sample still in *rem-1165*. At this point the resist is removed from the sample. Before proceeding to the next step of the process the sample surface is characterized by a *KLA Tenkor P-15* Surface Profiler, so that the effective etching thickness is known.

4. RIE O_2 (SiO_2-SURFACE CLEANING): 2min of reactive ion etching with O_2 is processed on the SiO_2-surface in order to clean it and make it more hydrophilic. Then an aqueous polystyrene nanoparticles solution used for the colloidal lithography process is spinned on the sample. In this way it is easier to obtain a self-assembled monolayer of nanoparticles[11], fundamental for a successful patterning of the point contacts. The cleaning process is made with these parameters: an O_2-flux of 20sccm (Standard Cubic Centimeters per Minute); the RF-Power (13.56 MHz) is 100W; the chamber pressure is 40 mTorr; the process chamber temperature is 30^oC and the sample is holded by a fused silica wafer (during all the RIE processes the temperature value and the wafer are always the same, if not differently specified).

5. NANOPARTICLES DEPOSITION: 5 drops of a 2% aqueous solution of polystyrene nanospheres[6] are dropt on the center of the sample (1.5x1.5 cm^2). Then a three-steps spin-coating process is executed: the first spinning is at 500 rpm for 10s, with the target of spreading the solution on the sample; the second one is at 1000 rpm for 30s, and it is at this point that the solvent and all the excessive particles are removed and the self-arrangment occurs; finally, a spinning at 2000 rpm for 10s, in order to remove possible remaining liquid on the sample edges. This particular procedure for the particles deposition and subsequent self-assembled close-packed monolayers obtaining has been well optimized in the work done by Marco Fischer (with the supervision of Dr. Adrian Iovan)[11] as bachelor student in this department, and also previously discussed by K. Ellinas et al.[12]. SEM images (Fig.4.2,4.3,4.4,4.5) made on the final hole-patterned metallic mask (see next steps) confirm the goodness of the process.

6. RIE O_2 (REDUCTION OF THE PARTICLES DIMENTIONS): a second step of 2min 45s RIE with O_2 is executed in order to shrink in size the deposited nanoparticles keeping constant the distance among them. The oxygen flux and the chamber pressure are the same of the previous step, but now an ICP (Inductively Coupled Plasma) RF-Power of 250 W is added to a RF-Power of 50 W. High gas pressure and low plasma power result in low energetic ions. According to this, the chamber pressure is kept high (40 mTorr) and the RF-Power is lower than before (50W instead of 100W). The result is an isotropic etching. The particles are etched on the top as well as laterally in an homogeneous way. The free O radicals start to attack the polymeric chains, then the non-ionized oxygen molecules O_2 complite the chain clevage. A possible reaction path is reported by M. Fischer in his report[11], and formally explained by S. J. Moss[13]. An accurate characterization [11] of this process by AFM technique shows how it is possible to tune the particles size by changing the time of etching. Measurements of nanopheres' height and diameter for different etching times have been done, and by fitting

[6] *microParticles GmbH*: Particle Size Standard 198 nm ± 6 nm; Standard Deviation 4 nm; 2% w/v aqueous suspension.

and extrapolating these data a diameter distribution around 15nm is expected for 2min 45s. This value is confirmed by the last observations by the SEM system on a metallic mask obtained after the current RIE step and subsequent metallization of the sample surface (see Fig.4.2,4.3,4.4,4.5).

7. Al-15nm DEPOSITION: the pattern of nanoparticles obtained in the previous step is now spatially frozen by depositing 15nm of Al on the top of the sample by e-beam evaporation. The thickness of the deposited layer is smaller than the nanoparticles height, so that they are mostly covered by Al, but not completely. The evaporation process is executed by the Edwards system, at a vacuum of $2\text{x}10^{-5}$mbar and a deposition rate of 0.7nm/s.

8. RIE O_2 (HOLES OPENING): the procedure for opening the channels where the point contacts will take place starts with this step. A reactive etching with O_2-flux of 20sccm, RF-Power of 100W, ICP-Power of 100W, and a chamber pressure of 50 mTorr is processed for 15min in order to remove completely the nanoparticles from the metallic layer. In this way a metallic negative of the nanoparticles mask is obtained.

9. RIE Ar (HOLES CLEANING): immediately after the opening of the holes, a reactive etching by Ar gives the opportunity to remove all the residual products of the particles etching reactions (carbons, for example). The constant flux of Ar in the chamber is 20sccm, the RF-Power is 100W, the ICP-Power is 100W, the chamber pressure is 50 mTorr and the process is run for 5min.

10. Ar-ION MILLING (HOLES CLEANING & METALLIC MASK OPTIMIZATION): for cleaning even further the holes and modelling the metallic mask, 7min of ion-milling are processed on the sample. With the same etching parameters reported in the step-2 it is known (by previous calibrations) that the Al-etching rate is around 1.5nm/min. We have also to consider that the previous 15min-reactive etching by oxygen has oxidized the surface of the Al-layer, and that the etching of Al_2O_3 is almost ten times slower than for Al (by calibrations). This means that in the first 4min is etched the 1nm-oxidized layer, and then about 5nm of Al are eroded. In this way the metallic layer is about 10nm, so that the apertures diameter reaches almost the effective nanospheres diameter. The desired metallic nano-mask needed for the point contacts array patterning is obtained. For seven minutes also the SiO_2 layer at the bottom of the holes is etched, but it is known (by previous calibrations) that the etching rate for SiO_2 is about 0.1nm/min. This means that the 15nm SiO_2 layer is only slightly etched in this step.

11. RIE CF_4 (HOLES-PATTERN TRANSFER TO SiO_2): a final reactive etching with CF_4 is executed in order to open the channels into the SiO_2-layer. A constant CF_4 flux of 20sccm, a RF-Power of 100W, a chamber pressure of 40mTorr and a resulting etching rate of 20nm/min (by previous calibrations) are the parameters for this 2min-etching process. The reactive etching of SiO_2 by CF_4 can be described in this way:

$$e^- + CF_4 \rightarrow CF_3 + F + e^-$$

$$SiO_2 + 4F \rightarrow SiF_4 + O_2,$$

where in the fist line is illustrated the formation of Fluoric-radicals by impact ionization with electrons and in the second line is illustrated the actual SiO_2 etching by the F-radicals. The last products of the reaction are volatile Si-compounds and oxygen, which are easily removed from the chamber by the pumping system. At the indicated etching parameters the etching rate is high enough to know that all the 15nm-layer is etched perpendicularly and that an undercut with an aspect ratio$\gtrsim$1 is obtained, due to the isotropic-character of the chemical etching process. On the other hand, the Cr-layer below is not etched at all, due to the high selectivity of the process (F-radicals do not react with Cr). Some images obtained with the *FEI Nova 200-Dual beam SEM/FIB System* clearly show the successfully patterned nanometric metallic mask (Fig.4.2,4.3,4.4,4.5).

12. FeCr-10nm DEPOSITION BY SPUTTERING (MAGNETIC PCs PATTERNING): before the deposition of materials, a 5min-plasma etching (data: RF-Power of 25W; pressure of 5 mTorr; Ar-flux of 20sccm) inside the main chamber of the sputtering system is processed on the sample, in order to have as much cleaned as possible holes just before to fill in them. A 10nm layer of FeCr is deposited with a rate of 0.103 nm/s (97s of deposition) with the sample placed on a rotating holder (the sample is always rotating during sputtering depositions for this specific work), a totat pressure of 5 mTorr, a constant Ar-flux of 25sccm and a DC-Power of 225W. The probability that sputtered material fly away form the target with a certaing angle with respect to the normal is not low. Furthermore, taking into account that the sample is not placed perpendicularly on the targets (see Fig.3.2) and is constantly rotating, it is not difficult to realize that actually the FeCr is deposited in the open as well as in the undercut regions. This was clearly shown by A. Gromov[14] by a SEM cross-section of a FeTaN/Cu/FeTaN multilayer with 0.5 μm undercut depth, produced in the same sputtering machine.

13. Fe-15nm DEPOSITION BY SPUTTERING (MAGNETIC PCs PATTERNING): a second deposition, this time of Fe, is done by the sputtering. A 15nm layer of Fe is deposited with a rate of 0.099 nm/s (151s of deposition), with a total pressure of 3 mTorr, a constant Ar-flux of 25sccm and a DC-Power of 75W. The real configuration of the patterned FeCr/Fe point contacts, according to what stated about the sputtering deposition above, is supposed to be similar to the sketch in Fig.4.6.

14. Cu-5nm DEPOSITION BY SPUTTERING: a last layer of Cu is deposited in the sputtering system. The parameters of deposition are: a rate of 0.033 nm/s (151s of deposition), with a totat pressure of 3 mTorr, a constant Ar-flux of 25sccm and a RF-Power of 120W. This layer is deposited in order to prevent the Fe-layer oxidation when the sample is taken out from the spattering system.

15. Cr-5nm DEPOSITION: 5nm of Cr are deposited by e-beam evaporation (Eurovac system) with a rate of 0.2 nm/s, at a pressure of 2×10^{-4}mbar. This thin Cr-layer is deposited in order to facilitate the sticking of the protective Au-layer.

16. Au-10nm DEPOSITION: 10nm of Au are deposited by e-beam evaporation (Eurovac system) with a rate of 0.2nm/s at a pressure of 2×10^{-4}mbar. This final Au-layer is deposited according to its non-reactivity with air's gases and chemicals. It acts as a protection-layer. It also makes easier the removing of the resist in the next photo-lithography processes.

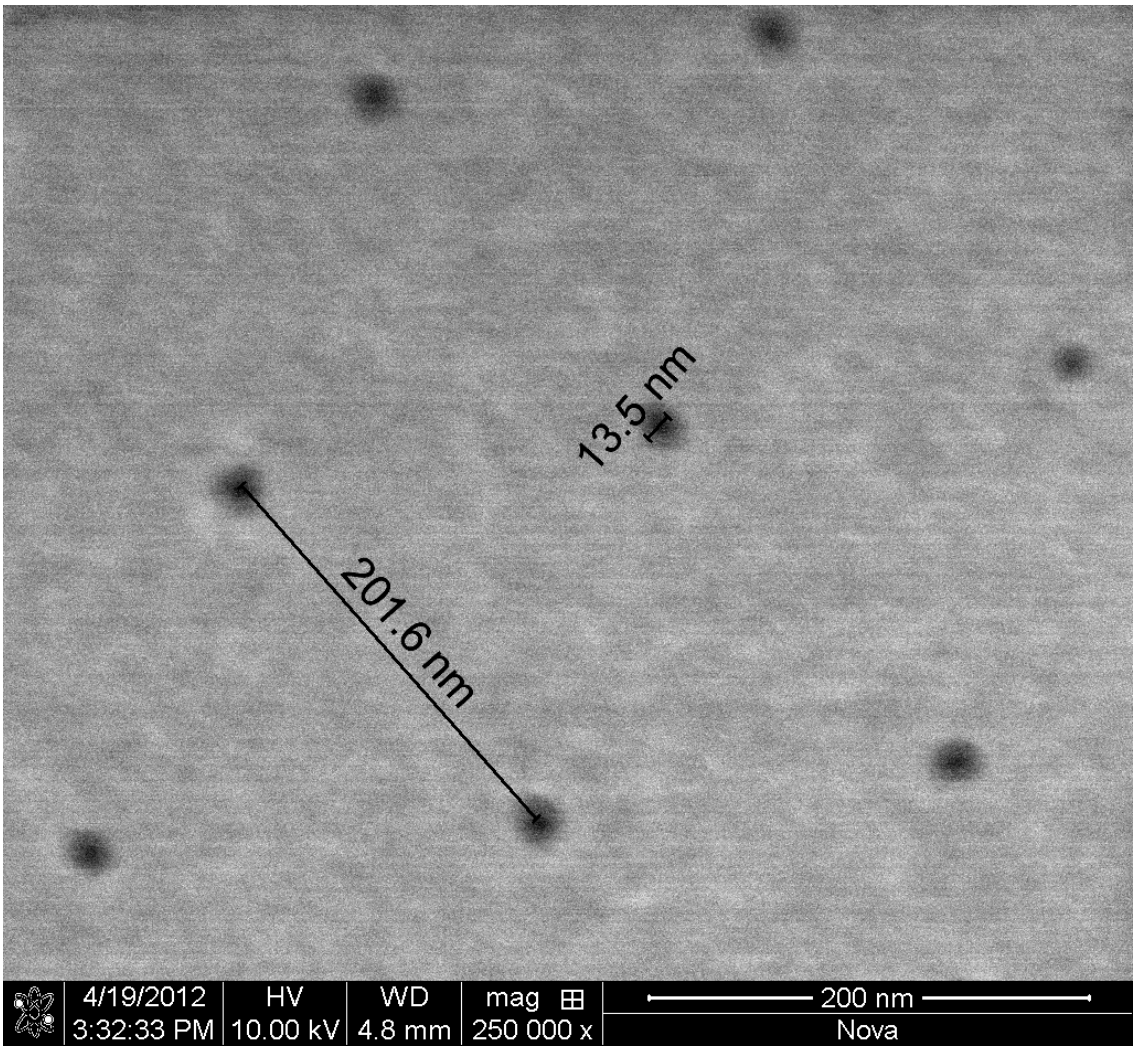

Figure 4.2: *SEM image of the nano-patterned Al-mask. We can see a clear image of the self-assembled hexagonal structure of the mask obtained by the colloidal lithography technique. We can see that the initial spacing between the particles is conserved ($\sim 200nm$) along all the dry etching and metallization processes, and that the obtained diameters size is below 15nm.*

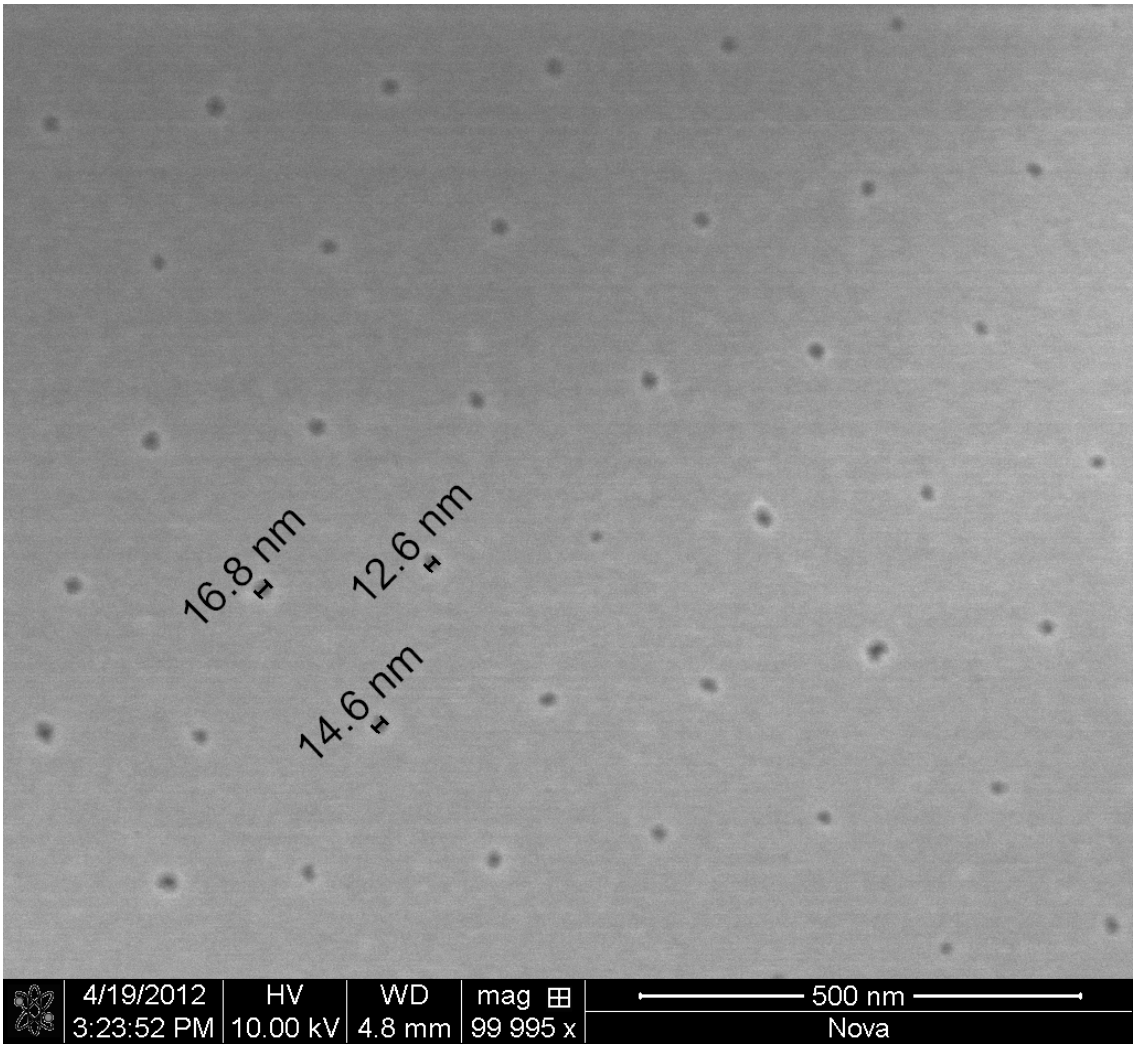

Figure 4.3: *SEM image of the nano-patterned Al-mask. In this image the distribution in the diameters size is illustrated. The diameters size is distributed around 14-15nm.*

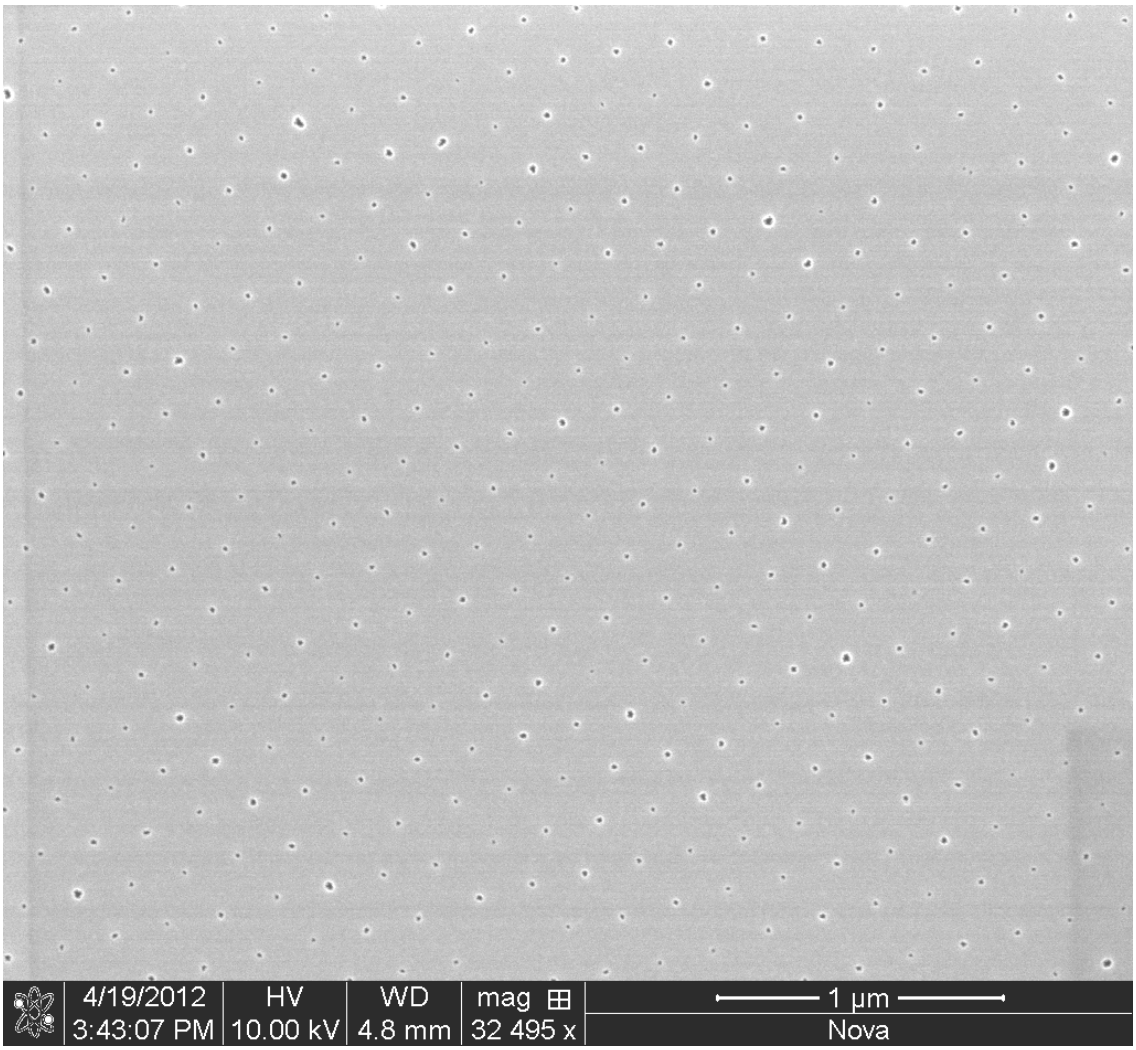

Figure 4.4: *SEM image of the nano-patterned Al-mask. The hexagonal structure is kept on areas of several* μm^2*. Furthermore, it is clear that actually there are two different distributions in the diameters size. One, that is also the more present in the image, is populated by holes with diameters of size around 15nm. A second one, less present in the image, has larger diameters values, around 20nm.*

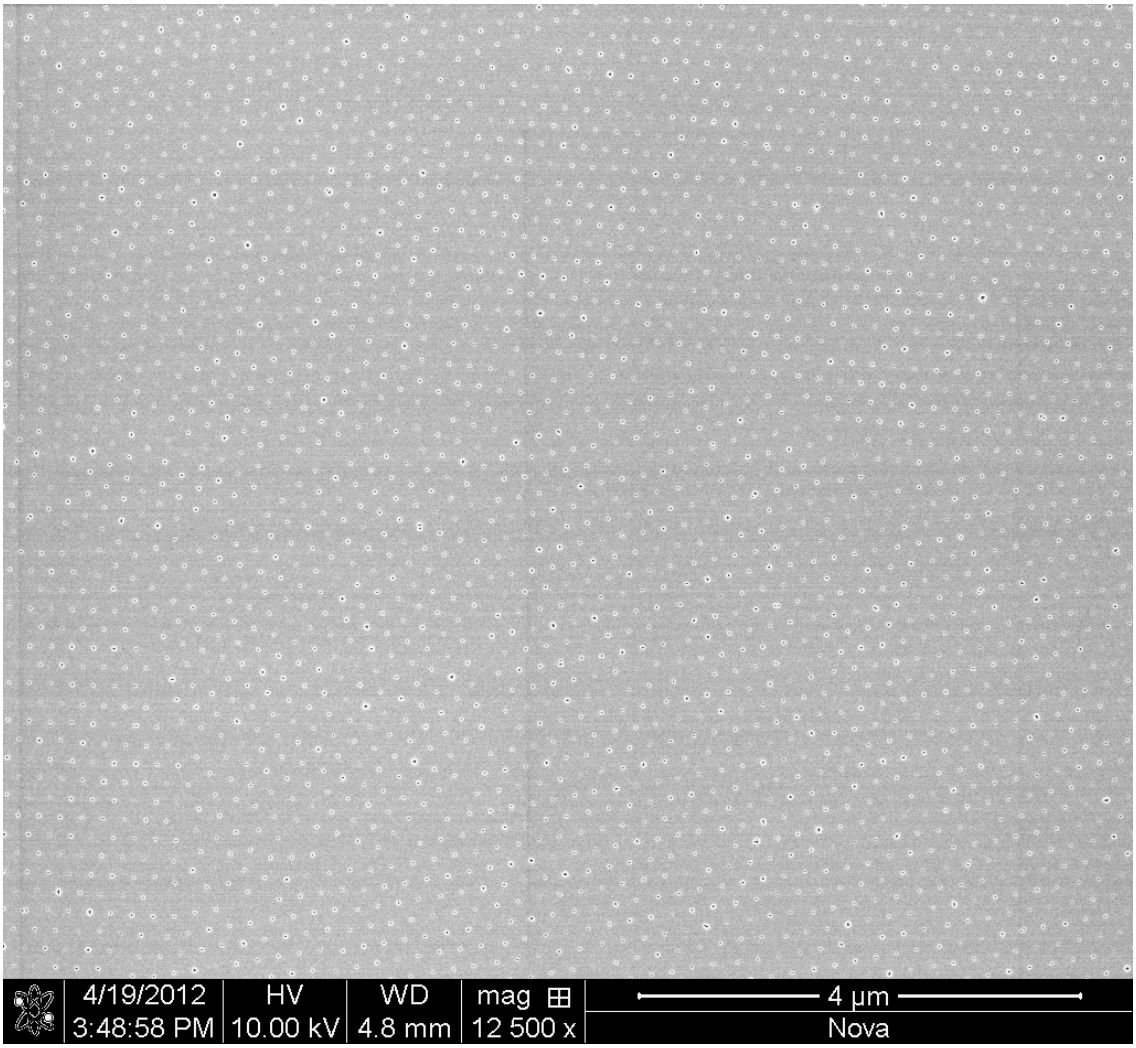

Figure 4.5: *SEM image of the nano-patterned Al-mask. We can see how, on the long-range, adjacent self-assembled structures are arranged in the mask.*

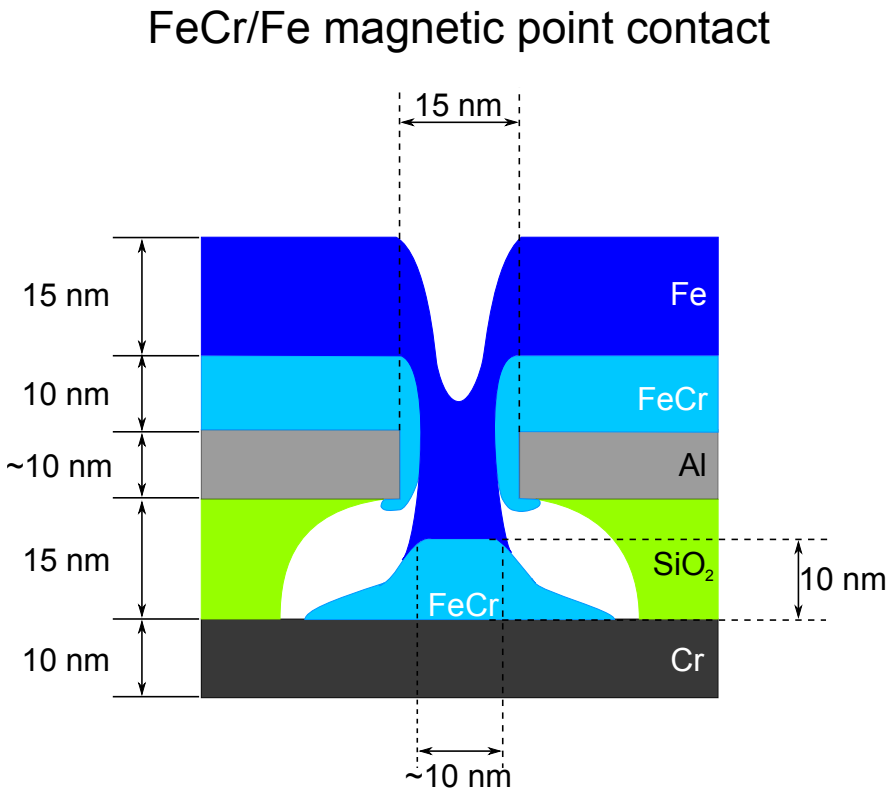

Figure 4.6: *Sketch of the section of one FeCr/Fe Point Contact. Starting from a diameter of 15nm for the hole in the Al-mask, the actual diameter for the magnetic point contact results smaller, around 10nm.*

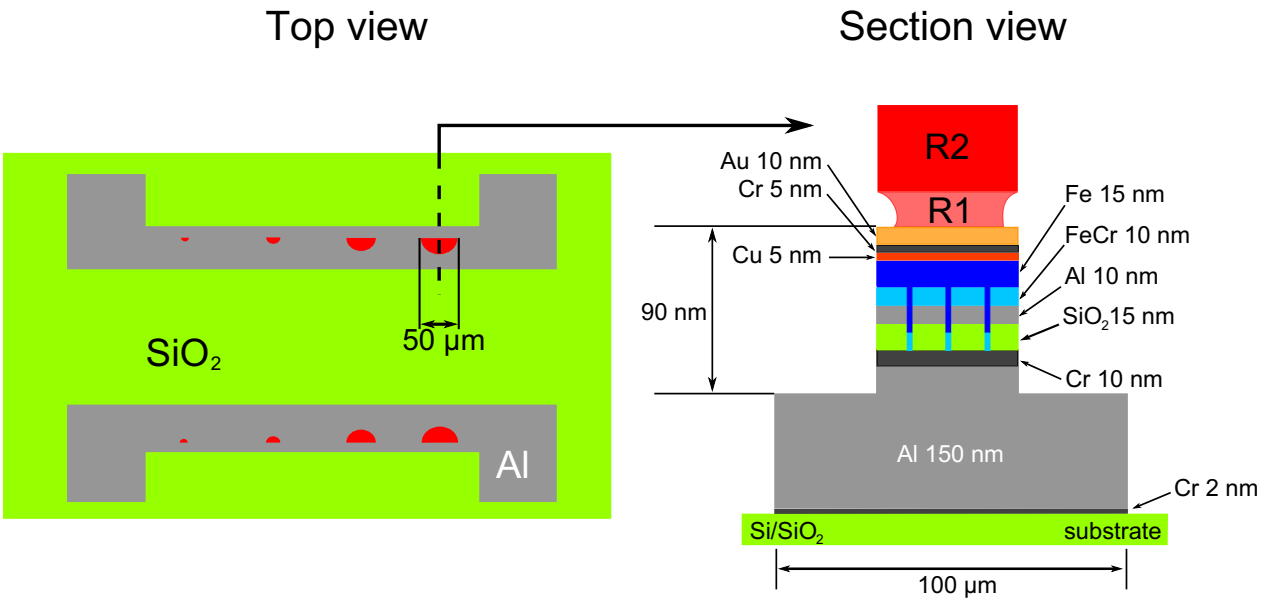

Figure 4.7: *Schematic of the patterning process for the half-disk resonators. The "top view" shows the resonators on the stripe-shaped bottom contacts after the ion milling execution, still covered by the double layer of resist on the top. On the right, a section of the patterned structure is clearly shown, with all the layers indicated. The array of magnetic PCs is embedded into the resonators, how it is supposed to be for the active material into a laser. Note that the figure is not in scale and the sizes of the different parts are not in the same proportion of the real structure .*

17. LITHOGRAPHY 2 (HALF-DISK RESONATORS PATTERNING): this photo-lithography process is identical to the previous one executed for the bottom-contacts patterning (see "LITHOGRAPHY 1"). The double resist technique is used again in order to have a $0.5\mu m$ undercut. This time the chromium mask used for the resist exposure is made by two parallel rows of half-disks. In one row the diameters of the half-disks go from $10\mu m$ to $50\mu m$ with an increase on $2\mu m$ from disk to disk. On the other row the diameters go from $9\mu m$ to $49\mu m$, with the same increasing from disk to disk. The two rows fit the two previously patterned bottom-contacts (see Fig.4.7).

18. Ar-ION MILLING (HALF-DISK RESONATORS PATTERNING): with the same parameters of the previous ion milling process, 70min of etching are executed on the sample. Two rows of half-disk resonators are patterned on the two bottom contacts (Fig.4.7). From measurements by the surface profiler it results an etching of about 90 nm.

19. SiO_2-40nm DEPOSITION BY SPUTTERING (INSULATION-LAYER): before the removing of the resist, an insulating layer of SiO_2 is deposited on the sample surface. In this way the Al parts of the bottom contacts as well as all the half-cylindrical pillars are electrically insulated with respect to the top-contacts which will be patterned in the final part of the whole process.

The deposition is executed with a rate of 0.022 nm/s (30min of deposition), a total pressure in the chamber of 3mTorr, an RF-Power of 150W.

20. LIFT OFF: the resist is removed with the same technique described at step-3. Differently from the previous case, now the undercut in the resist results to be very useful. The absence of resist just at the edges of the pillars avoids the deposition of material on the sidewalls of the resist, and the resulting vertical structures on the sample surface after that the resist is removed. In this way we get two good results : first, we do not have vertical structures coming out from the sample surface; second, it is much easier to lift off the resist and the material deposited on it from the sample.

21. LITHOGRAPHY 3 (TOP-CONTACTS PATTERNING): first of all is spinned *LOR-7B* (R1) at 5000rpm for 1min, and then baked at 190^oC on an hot plate for 5min. Then, the negative photo-resist *ma-N 1407*[7] (R2) is spinned at 4000 rpm for 1min and subsequently baked at 100^oC for 1min. At this point a chromium mask with the top-contacts pattern (see Fig.4.8, where the final structure of the sample is illustrated) is aligned by the mask aligner on the sample, which is exposed for 7.5sec to UV radiation. Finally, development process in the *ma-D 533/S Developer for Photoresists*[8] for 22sec. After checking at the optical microscope that no resist is still attached on the sample in the exposed areas, the sample is prepared for the Al-top-contacts deposition.

22. RIE O_2 (Au-SURFACE CLEANING): just before the Al deposition, the Au-surface at the top of the pillars is cleaned by reactive etching. Resist residuals from the lithography process as well as carbons present on the structures will be removed. The etching parameters are: O_2-flux of 20sccm, RF-Power of 100W, chamber pressure of 40 mTorr.

23. Al-200nm DEPOSITION (TOP-CONTACTS PATTERNING): the top-contacts are deposited by e-beam evaporation in the Edwards System. The deposition is executed with a total pressure into the chamber of 2×10^{-5}mbar, and a rate of 0.7nm/s.

24. LIFT OFF: the resist is removed with the same technique described at step-20. The comments reported during the description of the step-20 still hold.

25. BONDING PROCESS: now the sample is ready to be electrically connected to a PCB (Printed Circuit Board). By a *Kulicken&Soffa-4523 Digital Wire Bonder*, one of the two bottom contacts and four of the several devices are connected per time to a PCB in order to execute 4-points electrical measurements (IVC and Differential Resistance measurements) for each device.

Before going to the next chapter dedicated to the obtained experimental results, it is good to discuss a little bit more in depth the magnetic configuration into the PCs. The magnetic PCs are composed by FeCr and Fe. Fe is a majority ferromagnet. On the other hand, the alloy $Fe_{70}Cr_{30}$ here used is a minority ferromagnet[24]. In this particular alloy, the Cr-atoms change the internal magnetic configuration of Fe in such a way that the magnetization is reduced and the resistivity

[7] *micro resist technology GmbH* , Berlin-Köpenick, Germany.
[8] *micro resist technology GmbH* , Berlin-Köpenick, Germany.

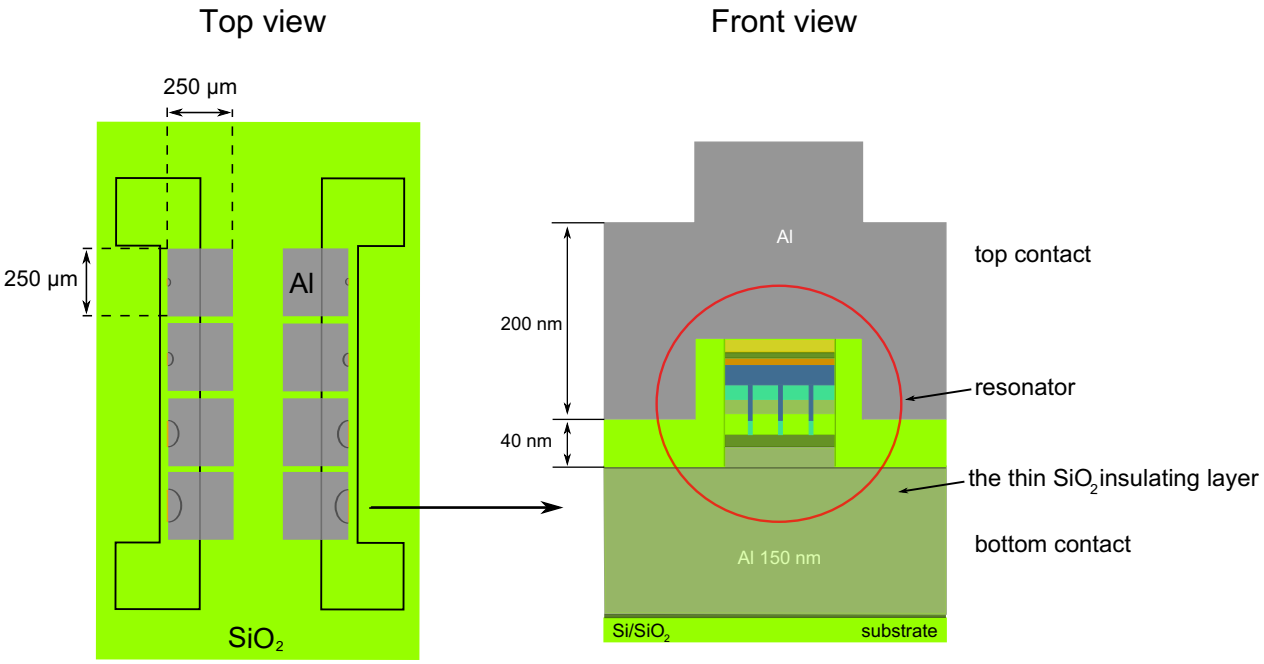

Figure 4.8: *Schematic of the final patterned device. On the left it is possible to see a sketch of the final structure of the entire chip, with bottom-contacts, top-contacts and half-disk resonators highlighted. On the right it is illustrated the front-edge of one of the 42 devices on the chip. An insulating coating layer covers all the chip but the top-contact. From this edge will be possible to detect the radiation, as shown by Monakhov et al.[8]. Note that the figure is not in scale and the sizes of the different parts are not in the same proportion of the real structure .*

of the majority electrons is increased. So, the electrons with higher conductivity are the minority ones now. Due to the repulsive potential of the Cr impurities[23], the majority conduction electrons are now also the ones which populate the spin-band with higher energy. At the same time, the parallel (P) configuration between the Fe and the FeCr magnetizations into the PCs is supposed to be obtained due to the exchange interaction at the interface between the two metals. All the theoretical requirements about the magnetic configuration inside the PCs are satisfied in order to produce photons by spin-flip dis-excitation of the electrons. An highly spin-polarized current is injected from Fe to FeCr with a subsequent pumping of the upper spin-band into the alloy, so that a spin-population inversion is supposed to be obtained. The Curie temperature T_C of the used FeCr-alloy is around 500^oC, which results in a threshold voltage of around 60mV, according to the relation:

$$V_{th} \approx \frac{k_B T_C}{e}, \tag{4.1}$$

where k_B is Boltzmann's constant and e is the charge of the electron.

Chapter 5

Measurements technique and experimental results

At the beginning of this chapter I will briefly describe the experimental set-up used for electrical measurements. The obtained experimental results will be presented and compared with results from previous works. Similarities with experimental results obtained in single point contact measurements will be shown, and new other interesting ones will be presented.

5.1 Electrical measurements technique

Electrical measurements are made on different samples, obtaining their IVC (current-voltage characteristic) as well as their differential resistance dV/dI. In this way it is possible to investigate the transport properties of the sample and the physical phenomena involved. The evidences of interaction of electrons injected into point contacts with phonons and magnons, as well as of spin-transfer-torque effects are all contained in the *dV/dI*- and in the resistance *R*-characteristics of the sample.

For the measurements of the current I_S and the voltage V_S on the sample is enough to measure them directly from the sample, by multimeters. While, in order to obtaine the differential resistance a lock-in technique is needed. Supplying to the sample a DC-current I and a modulating AC-current $icos(\omega t)$ with the amplitude $i<<I$, the AC-current is used as reference signal in the lock-in filter. Taylor's series expansion (at the second order in i) of the voltage V on the sample as function of the total applied current $I+icos(\omega t)$ is [4]:

$$V(I+icos(\omega t)) = V(I)+\frac{dV}{dI}icos(\omega t)+\frac{1}{2}\frac{d^2V}{dI^2}i^2cos^2(\omega t) = V(I)+\frac{dV}{dI}icos(\omega t)+\frac{1}{4}\frac{d^2V}{dI^2}i^2(1+cos(2\omega t)). \tag{5.1}$$

It is clear now that the dV/dI can be obtained by extracting the ω-component from the whole V. Using a lock-in filter with reference signal at the same frequency ω this is possible. The amplitude of this ac signal turns out to be proportional to the differential resistance of the sample.

The electrical circuit used for the samples characterization is illustrated in Fig.5.1. A DC-voltage V_0 is supplied by the function generator *KEITHLEY 2601A System SourceMeter*. The DC source consists of a triangular voltage function with frequency of 1 mHz. There was the possibility to apply

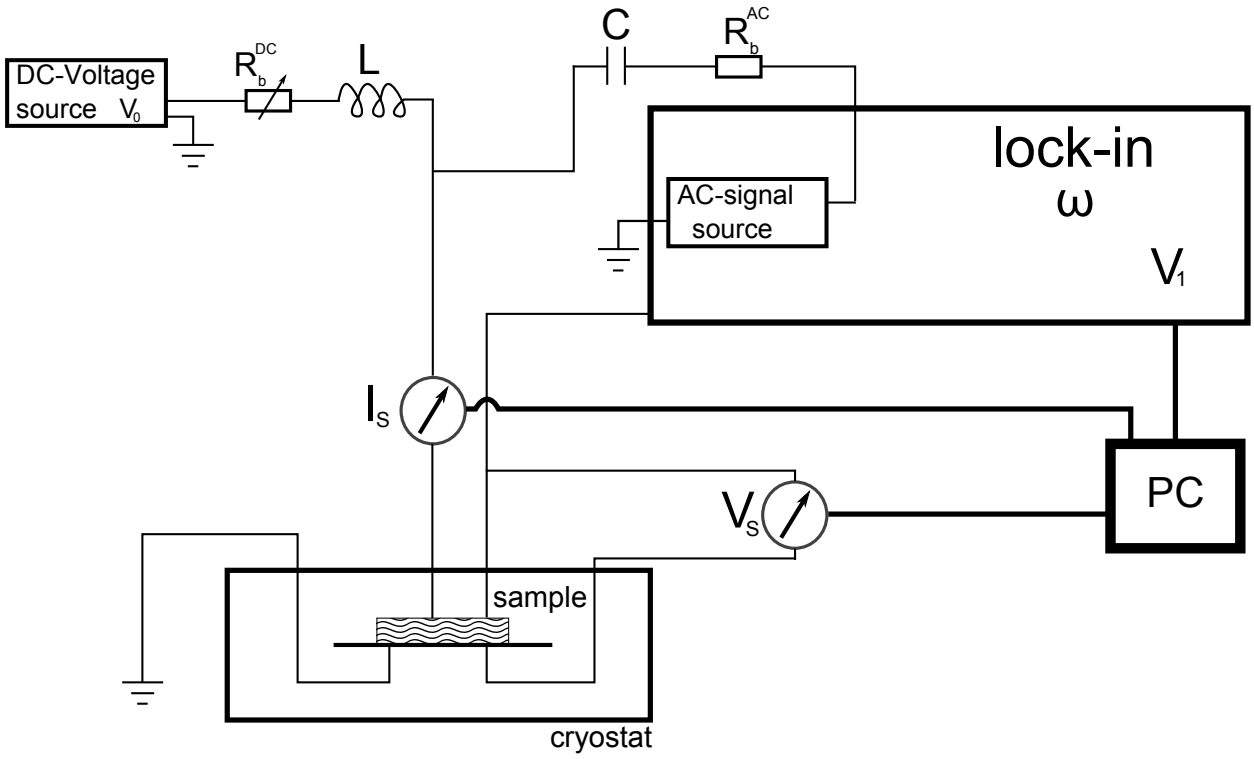

Figure 5.1: *Schematic of the measurement set-up for electrical characterization of the sample.*

a voltage up to 40V. An AC-signal is also supplied to the sample directly by the lock-in system, a *Standford Research-SR830 DSP Lock-in Amplifier*. Its amplitude is controlled by the R_b^{AC}, in order to be always much smalled than the DC value. Its frequency is fixed to $\omega/2\pi$=483 Hz. This signal is also used as reference signal for the lock-in technique. The DC voltage and the AC signal are coupled by an LC circuit and supplied to the sample. The voltage V_S and current I_S through the sample are measured by two DC *KEITHLEY 2000 Multimeters*, in the 4-points measurement configuration. The dV/dI ($V_1 \propto$dV/dI, in Fig.5.1) characteristic is measured by the lock-in system. All instruments are connected to a PC via GPIB (General Purpose Interface Bus≡IEEE-488), where the data are read out and stored. A computer software designed in the Lab-View environment is used for data acquisitions. Electrical measurements have been done at room temperature as well as at low temperature (liquid nitrogen, 77K).

5.2 Experimental results from previous works

Before illustrating the experimental results obtained on the samples fabricated in the nano-lab, it is useful to have an overview of the experimental results obtained by other researchers investigating magnetic point contacts. In this way we will compare directly our obtained results with the previous ones.

For our work two experimentally observed results are interesting: Spin Torque-Driven Excitations (STDE) and Current-Induced Hysteretical Switching (CIHS) mechanisms in single N/F interfaces (in our case, the interface between the two composing materials of the PCs). Unfortunately no previous results are available about a full magnetic point contact (F_1/F_2). Who would like to go more in depth in the theoretical aspects can consult the reference[17].

A current-induced STDE in single PC between a normal metal N and a ferromagnet F was for the first time experimentally observed by Ji et al.[18] (2002), where a nanometric Ag-tip was in contact with a Co film. The evidence of the STT was a peak in the measured differential resistance dV/dI of the PC. About one year later Stiles et al.[19] presented a phenomenological theory for explaining these magnetization instabilities in single N/F interfaces driven by unpolarized current from N to F. According to them, in order to obtain this kind of magnetization instabilities into the ferromagnet is fundamental to produce a large spin-accumulation at the interface, in the normal metal. This is possible only if there are enough impurities in N close to the interface, that act as back-scattering centers for the electrons reflected at the interface due to the different conductivity for the majority and minority spin-channels in F. If it is present also a non-omogeneous magnetization distribution, the STT mechanism can occur, resulting in an increasing of the resistance in the PC. So, the diffusive regime for the electrons in the PC is one of the conditions to make it happen. A clear image of the STT in N/F interface is the one in Fig.5.2, after A. Konovalenko et al.[20].

A different mechanism gives us an other phenomenon, the CIHS in the resistance R(I) of the PC with a single N/F interface. It was observed and discussed for the first time by T. Y. Chen et al.[21] (2004). In Fig.5.3a is reported their experimental observations of hysteresis loops for R-I and dV/dI-I in a Co/Cu(tip) PC. This "spin-valve" effect (it is well known the hysteretical behavior of R(I) in F/N/F spin valves) needs a different explanation. A. Konovalenko proposed as origin of this effect the formation of energetically distinct surface spin states[17, 22]. In this new model the magnetic thin layer is supposed to be composed by two weakly coupled magnetic sub-layers: a surface layer and a "bulk" layer. By injecting the current from N to F or from F to N it is possible to align or anti-align the magnetization in this two layers, located at the PC core, where the current density reaches its maximum. An experimental observation of CIHS in N/F PCs by I. K. Yanson et al.[22] is reported in Fig.5.3b.

5.3 Experimental results

First I will present some images with the respective descriptions of the chips fabricated in the nano-lab. Will be also presented the results of electrical measurements done on our samples.

5.3.1 Fabricated samples

During these six months of work in the nano-lab different samples have been fabricated. Chronologically speaking, the first ones were characterized by full-disk resonators, with a contacts-configuration optimized for 4-points electrical measurements. As we can see in Fig.**??** the bottom contact is S-shaped, with seven devices patterned on it. The cylindrical resonators are completely coated by the metallic top-contacts. The top-contacts extend on the whole chip area, in order to facilitate the bonding to a PCB (Printed Circuit Board) for the electrical measurements. In Fig.5.5a and Fig.5.5b is shown more in detail the structure of the resonators. Two different chips have been patterned

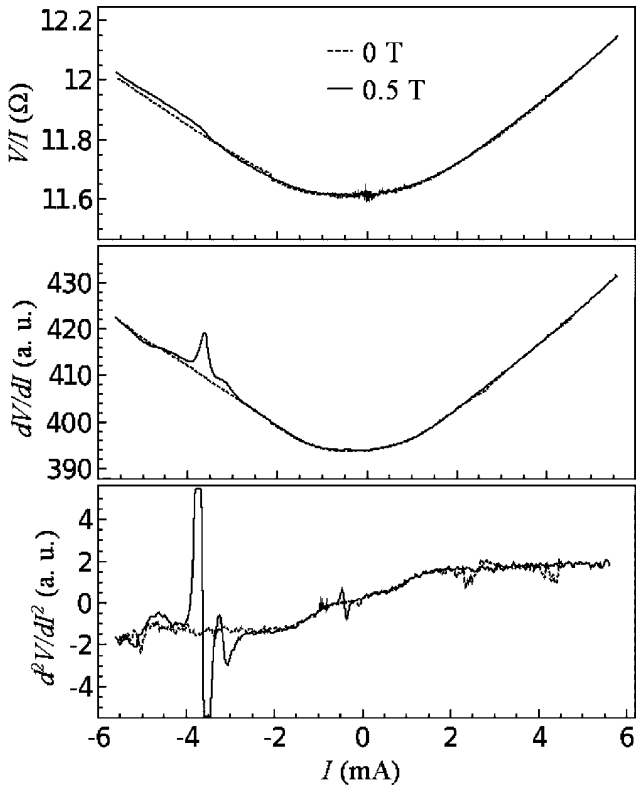

Figure 5.2: *V/I, dV/dI and d^2V/dI^2 vs I for a Cu(20nm)/Co(5nm)/Ag(tip) point contact, after A. Konovalenko et al.[20]. Here it is clear the step-like and the peak-like character of STT respectively in the V/I and dV/dI characteristics of the N/F PC. The effetc is seen only when an external magnetic filed H is applied perpendicularly to the Co surface. The author explains this with the necessity to produce the favorable magnetization configuration for the instability generation.*

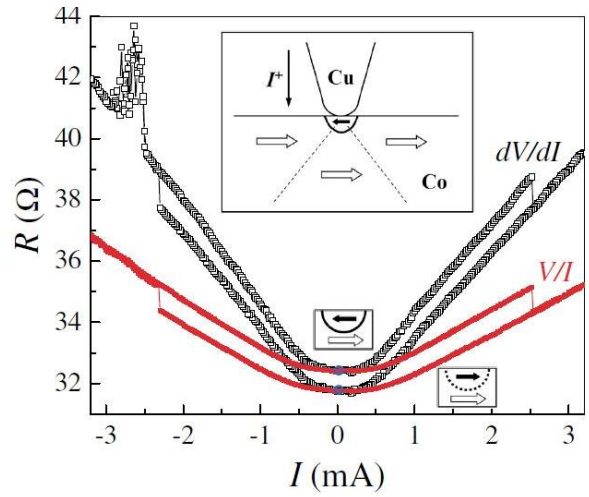

(a)

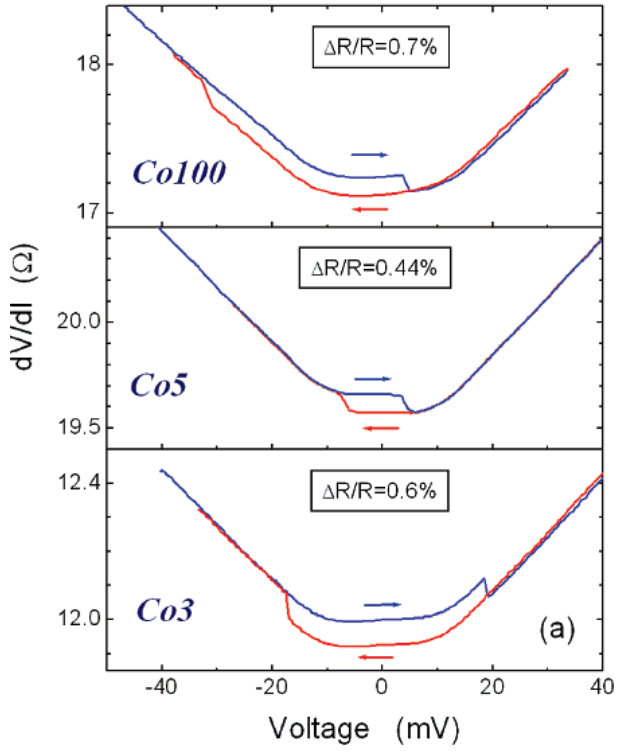

(b)

Figure 5.3: *Two examples of current-induced hysteresis loops for N/F PCs, observed in previous works. In (a) hysteretical current-induced switching loop for a Cu tip in contact with a single Co layer. In the inset are schematically shown the model and the spin structure at zero bias. After T. Y. Chen et al.[21]. In (b) hysteresis in dV/dI for PCs with Co films of varying thickness, after I. K. Yanson et al.[22].*

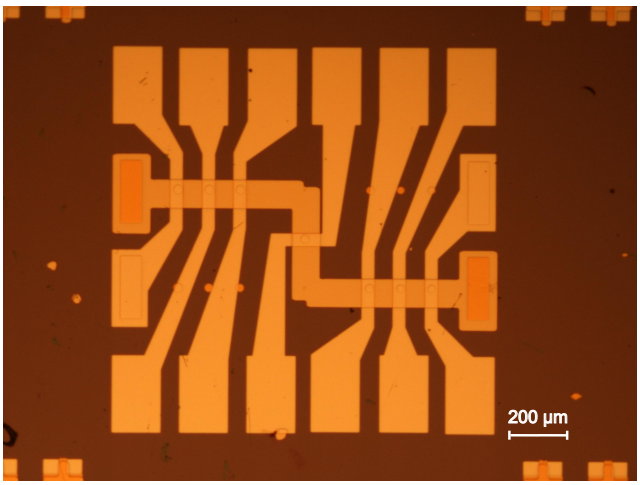

Figure 5.4: *Full-chip image of the full-disk devices configuration. The image is magnified 5 times and obtained by a Nikon DS-5M camera (5 Mpix) mounted on a Nikon DIC ME600 microscope. Magnification range: 5× to 100×.*

with this configuration: one with Fe/FeCr (F_1/F_2) PCs; a second one with Cu as filling material, so that Cu/Cr (N/N) non magnetic PCs have been obtained. The second sample has been fabricated in order to compare the results obtained from it with the ones obtained from magnetic samples.

The last fabricated sample has a different configuration with respect the previous ones. It is exactly the result of the patterning process described in Chapter 4. As it is possible to see in Fig.5.6 the bottom- and top-contacts have a different geometry as well as the resonators, which are half-disk-shaped now. On the chip there are two stripe-shaped bottom-contacts, on which there are 42 resonators of different sizes. On one side the resonators diameters go from $10\mu m$ to $50\mu m$, with a step of $2\mu m$ from resonator to resonator. On the other side the resonators diameters go from $9\mu m$ to $49\mu m$, with the same step. In the picture is not reported all the chip, but only the final part of one row. The reason is the large size of the full chip, about 6 mm in length. It was impossible to take a picture of the full chip by the microscope.

In Fig.5.7a and Fig.5.7b are shown two devices with differen size: a $50\mu m$ in diameter and a $12\mu m$ in diameter resonators respectively. The resonators are only partially covered by the metallic top-contacts. The flat edge of the devices is not covered by aluminium, and the reflection process is due only to the different refractive indeces for the dielectric and the air. This configuration is supposed to be optimal for the detection of the emitted light. In this chip the nano-channels are filled in with $Fe_{70}Cr_{30}$ and Fe, so that the magnetic hetero-PCs (F_1/F_2) have been obtained.

5.3.2 Electrical measurements

Different samples with different materials and different shapes for the resonators have been patterned and investigated. As first, will be shown the experimental results obtained by a sample with non-magnetic point contacts (Cu/Cr). In Fig.5.8 we can see that the shape of the differential resistance

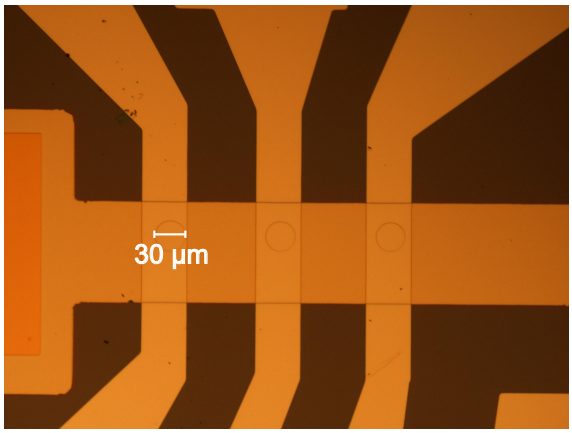

(a)

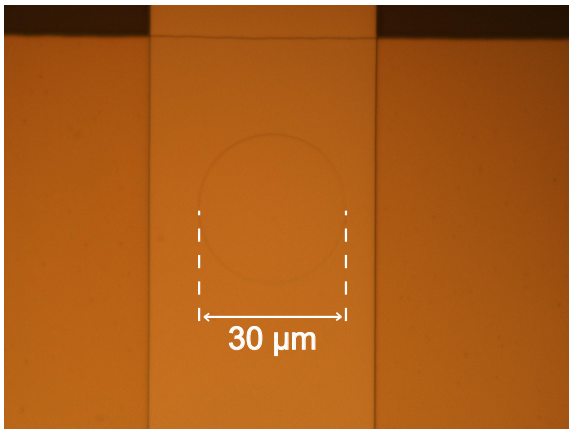

(b)

Figure 5.5: *Images of full-disk resonators obtained by Nikon DIC ME600. In (a) an image of some full-disk resonators on the chip, magnified 20×. In (b) an image of a single full-disk resonator on the chip, magnified 100×.*

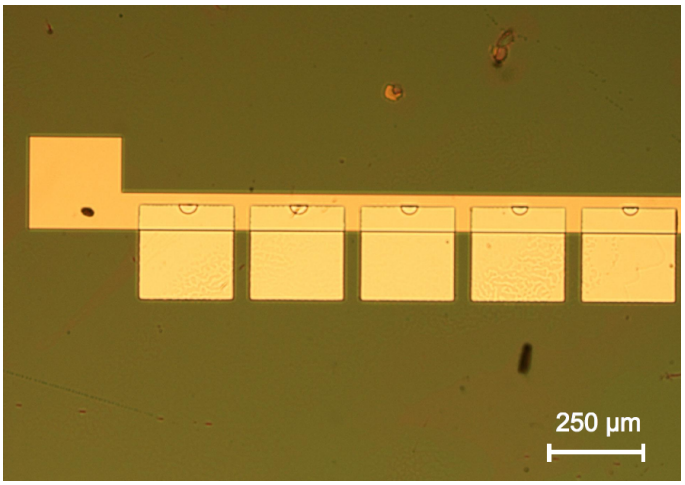

Figure 5.6: *Image of part of the chip with the halfl-disk devices configuration, magnified 5×. Image obtained by Nikon DIC ME600.*

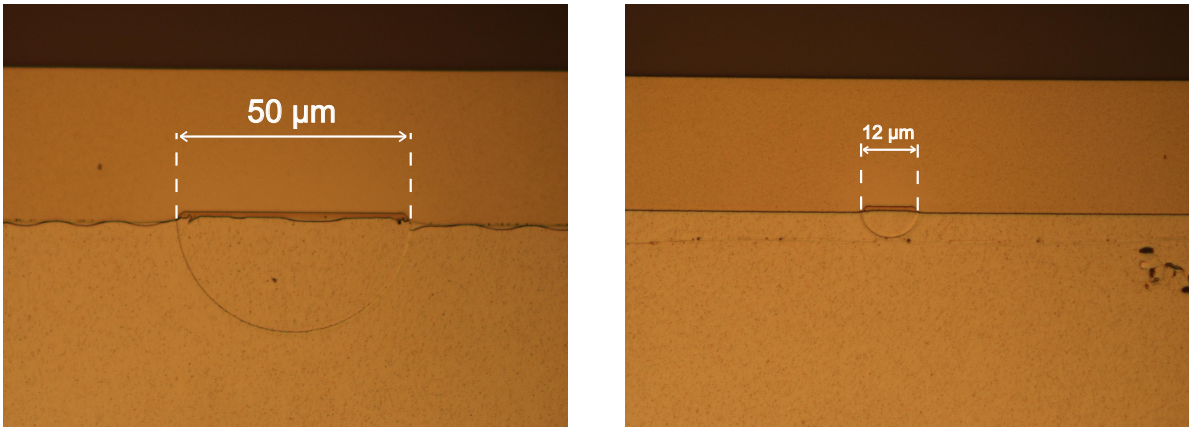

(a) (b)

Figure 5.7: *Images of half-disk resonators, obtained by Nikon DIC ME600. In (a) an image of a half-disk resonator with a diameter of 50µm, magnified 100×. In (b) an image of a half-disk resonator with a diameter of 12µm, magnified 100×.*

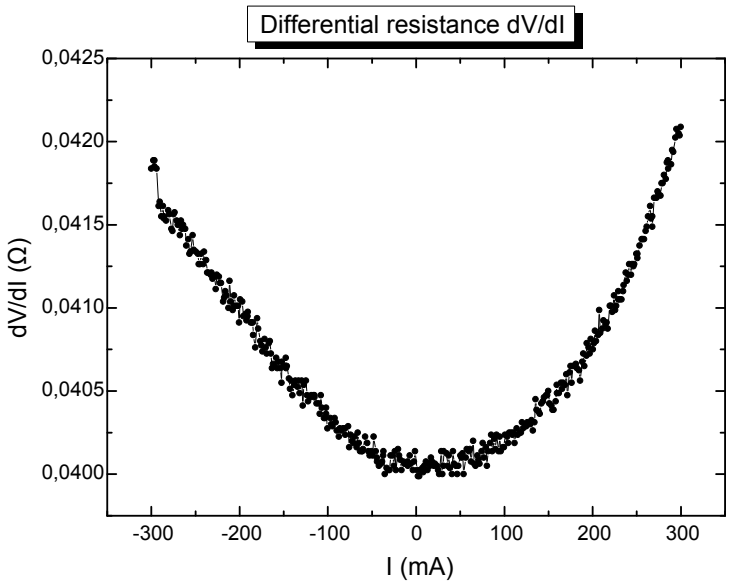

Figure 5.8: *Measured differential resistance of a non-magnetic-PCs device. The typical parabolic behavior for PCs is recognizable. No particular excitations are visible.*

dV/dI characteristic as function of the bias current I is parabolic. This is a typical behavior of PCs-differential resistance, as also shown in Fig.5.2 and Fig.5.3. It means that the structure obtained is actually working like an array of metallic PCs. The value of the resistance at zero bias is R=0.04Ω. Thinking to have point contacts with a size of 10nm in diameter, according to the SEM images of the nano-patterned mask (see Fig.4.3) and the supposed structure of the patterned PCs in the sputtering machine (see Fig.4.6), we have a rough estimation of 250 PCs working in parallel ($R_{PC} \simeq 10\Omega$ for d=10nm, according to the expression of a single PC resistance given in paragraph 2.1.1). This is a direct proof that the colloidal lithography technique used for patterning the array of PCs works. On the other side, no evidences of excitations are visible in the measured dV/dI for this non-magnetic sample.

After this "test-" non-magnetic sample, devices with magnetic PCs have been fabricated and investigated. Here are shown the results obtained by a sample with $Fe_{70}Cr_{30}$/Fe PCs and half-disk-shaped resonators. How is shown in Fig.5.9a a clear CIHS is obtained in the resistance of this device. The magnetoresistance is about MR=2.3%. This is very similar to what was obtained by T. Y. Chen et al.[21] and subsequently by Y. K. Yanson et al.[22] on sigle magnetic PCs. In our case the hysteresis loop is only on the side of positive current bias. The bias-current at which the effect occurred in single PCs configuration is around 2-3mA[21]. In our case the values are about 200 times higher. With a resistance of the device of 0.016Ω (see Fig.5.9a), we can roughly estimate the number of working PCs around 500 (with PCs with resistances around or below 10Ω). This is a direct demonstration that at least hundreds of PCs are working in parallel.

In Fig.5.9b is reported the IVC of the device. The hysteresis loop is visible in the inset of the figure, where it is clear that for increasing current the value of the voltage on the device is lower

than the one for decreasing current. In the IVC is also possible to see the low non-linearity due to the thermal increase of R. The maximum measured voltage on the device is 8.5mV. This value is an eighth of the supposed threshold voltage for the lasing effect of about 60mV. It means that if we want to find some evidences of stimulated photons emission we have to increase the bias further. The problem is that, if we assume that actually 500 PCs are working, the injected current density into the PCs is about 10^{10}A/cm^2. This is more or less the typical value of current density used also in previous works on PCs, where no heating problems have been obtained ($\sim 10^9$A/cm^2[20]). However, an increase of the bias of one order of magnitude could be enough to give us a serious heating into the devices, with subsequent burning of the sample. Actually we have obtained in a few occasions the burning of devices due to high bias currents. So, every time during the measurements the bias has been increased step by step, starting from low values. This has been done in order to not damage the devices and also to start with the detection of the common magnetic excitations. Then, the bias is increased further in order to verify if some new kind of non-linearities can be detected in the IVC close to the supposed threshold condition.

Finally, it is relevant to report that during more recent measurements, which have been done during the report drafting, very interesting results have come out. Very large excitations in the IVC of a few samples have been recorded. A two-fold increase in the resistance has been measured, with a threshold feature typical of a laser. These last results make us think that probably in these devices a stimulated emission of light has actually occurred, but still further measurements on new samples are required in order to be sure that this is something related with the lasing effect.

5.4 Possible interpretation of the CIHS effect

It is possible to explain the measured CIHS effect as a spin-torque effect at the interface FeCr/Fe. Starting with the supposed P (parallel) configuration for the magnetizations into the two materials, injecting a spin-polarized current from Fe to FeCr it is possible to have a spin-accumulation at the interface due to the higher resistivity experienced by the majority electrons entering the alloy (see Fig.5.10). As shown also in Fig.5.10, the magnetic moment accumulated at the interface is aligned with the two magnetizations of the metals, so that no spin-torque can be generated by the spin accumulation. On the other hand, when electrons are injected from FrCr to Fe are the minority electrons that are reflected at the interface, attempting to enter the Fe layer. In this case the spin-accumulation generates a magnetic moment anti-aligned with respects the two magnetizations, so that when the current density is high enough a STT effect can occur. A thin layer with inversed magnetization can be obtained at the interface, generating two domain walls. This gives us an higher resistance for the PCs and so for the entire structure, since the resistance experienced by an electron flowing through a domain wall is always higher than in the absence of it. Then, when the current comes back to lower values, the intrinsic magnetization configuration of the PCs is again energetically favored and the resistance goes back to the starting value. This simple model gives us an explanation for the MR-effect, and it explains also why the effect is present only at positive bias. Anyway, further investigations are needed to clarify what really is the origin of the magnetoresistance in this F_1/F_2 PCs interface. For now we only show the experimental results, trying to understand if there are clear evidences of light production, and we know that one evidence is the increase of the device resistance, according to Kadigrobov et al.[5].

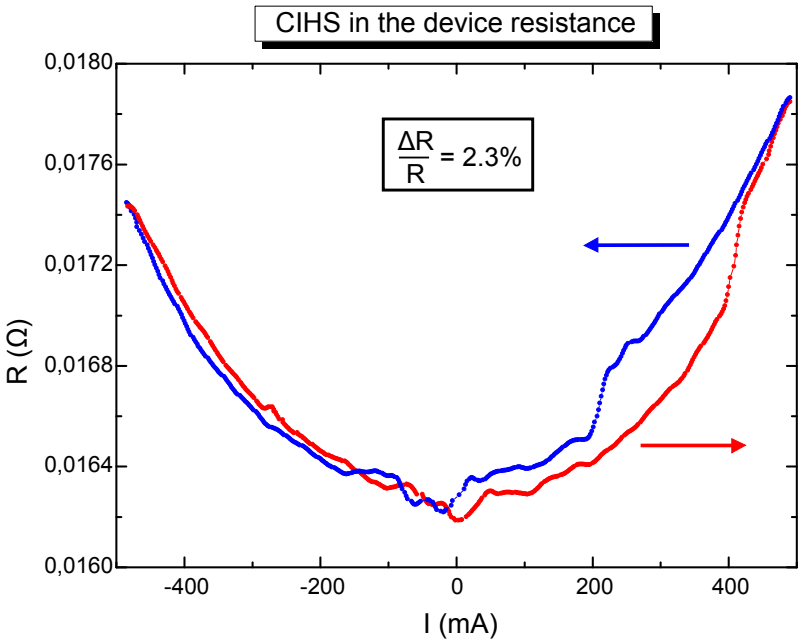

(a)

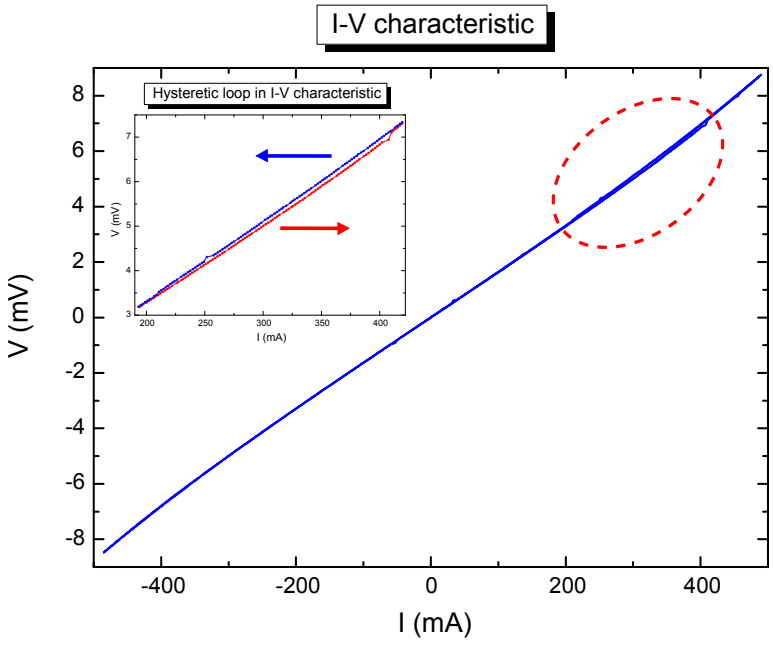

(b)

Figure 5.9: *Measured resistance and IVC of an $Fe_{70}Cr_{30}$/Fe-PCs device with half-disk-shaped resonator. In (a) the measured CIHS in the resistance of the device. The asymmetry in the resistance could be linked with the specific magnetic structure in the PCs. In (b) the measured IVC of the device. In the inset, it is clearly visible the result of the hysteresis loop on the IVC due to the MR-effect measured in the resistance of the device.*

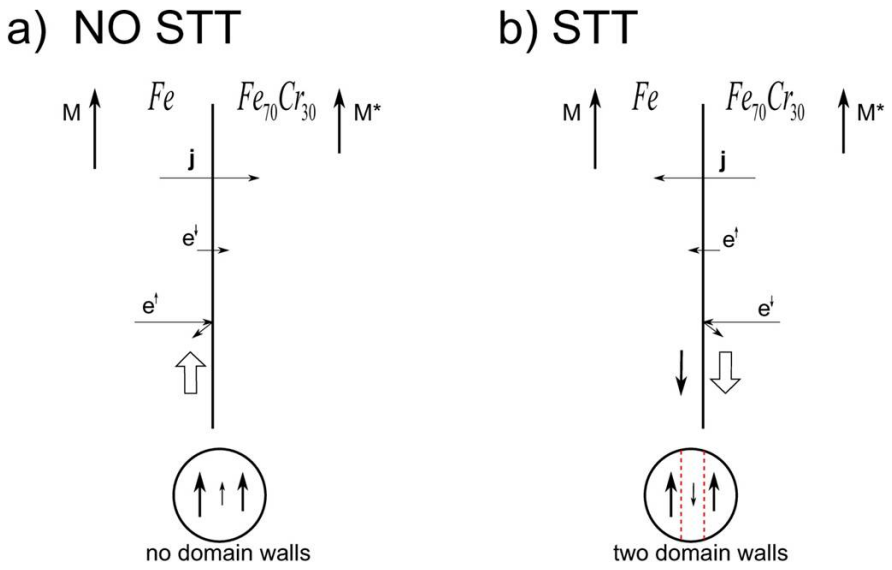

Figure 5.10: *Sketch of a possible model for the MR-effect recorded in our samples.*

Chapter 6

Conclusions and Outlook

A process for the patterning of an array of point contacts (around 10nm in diameter) has been developed. The use of colloidal lithography technique, joint to the traditional photolithography technique has made possible the patterning of a proposed magnetic PCs-based optical resonator. Devices of different shapes, with $Fe_{70}Cr_{30}$/Fe PCs have been patterned and investigated. From the analysis of the measured IVCs, resistances and differential resistances of some of the patterned devices is possible to recognize typical magnetic behaviours of magnetic PCs, like for example a hysteresis in the resistance. Additionally, have been recorded also other interesting behaviors in the most recent measurements. Large non-linearities have been detected in the IVCs. The large excitations occurred only for high bias voltages, where the voltage across the sample is comparable or larger than the theoretical threshold value. However, still further measurements are required in order to clarify the real origin of the new measured excitations. In order to clarify if the described results are actually due to photons production or not, optical measurements are needed. The detection of emitted radiation by the sample in the terahertz-range of the electromagnetic spectrum (after filtering of the partially superimposed thermal IR-radiation) would be a strong evidance of the desired lasing effect.

Chapter 7

Acknowledgements

If in these last six months I have had the opportunity to work on and learn about this project is mainly due to two persons: the professor Vladislav Korenivski, chief of the Spintronics group at the Applied Physics department at KTH; and the researcher Dr. Adrian Iovan. Professor Korenivski gave me the opportunity to join his group, so that I have had the chance to work on a fascinating as well as complex project, with a lot of physical features which have been stimulating my scientific curiosity along all these months. He has been always willing to clarify my doubts, making me understand more and more in depth all the features of the project. Every time, after each discussion we have had in his office, I have felt a richer man. I desire to thank him for all this. On the other hand, Adrian taught me all the lab-skills needed for this project. Every day he has driven me during my lab-work, showing me new experimental techniques or telling me how to improve the ones already learned. He has been always open to answer to the tones of questions I used to ask him. For all these and other things, I want to thank him. He has been a great teacher, a precious colleague and also a good friend. I want also to thank Dr. Anatolii Kravets, who helped me to better understand the functioning of some of the machines used in the nano-lab and with whom I have had nice discussions about Physics. I would like to thank also Prof. Marco Finazzi, for accepting to be the supervisor of my thesis at my home university. Then I would like to say "thank you" to my office colleagues, over all to Ann-Katrine and Michael. They have helped me with their computer skills, which have turned out to be very precious for the drafting of my report. They have also made my time in the department a great time, with funny discussions about the most "useless" things. The discussion about the difference between Citron, Lime and Lemon is destined to become legendary. I want to say thank you to my friend Arezoo, that with her liking and personality has made my coffee-breaks special. Thank you Arezoo for this and for much more. I wish you the best for your master thesis in photonics and I hope your relation with the spectrum-analyzer will become more friendly. Then, many thanks to my old and precious friends Stefano and Mattia, that like always have been here with me also this time, in Stockholm, to share with me the important moments of my life. Finally, I would like to thank my family, which has always and constantly supported me and believed in me more than I did. Per questo e per una infinità di altre ragioni: grazie mille Mamma, Papà, Oscar, Davide e si, anche tu Silvia. Senza di voi tutto questo non sarebbe stato possibile.

Bibliography

[1] G. Binash, P. Grünberg, F. Saurenbach and W. Zinn: "Enhanced magnetoresistance in layered magnetic structures with antiferromagnetic interlayer exchange", *Phys. Rev. B*, vol. 39, no. 7, pp. 4828-4830 (1989).

[2] M. N. Baibich, J. M. Broto, A. Fert, F. Nguyen Van Dau and F. Petroff; P. Etienne, G. Creuzet, A. Friederich and J. Chazelas: "Giant Magnetoresistance of (001)Fe/(001)Cr Magnetic Superlattices", *Phys. Rev. Lett.*, vol. 61, num. 21, pp. 2472-2475 (1998).

[3] W. J. Gallagher, S. S. P. Parkin: "Development of the magnetic tunnel junction MRAM at IBM: From first junctons to a 16-Mb MRAM demonstrator chip", *IBM J. Res. & Dev.* Vol.50 No.1 January 2006.

[4] Yu. G. Naidyuk, I. K. Yanson: "Point-Contact Spectroscopy", *Springer Series in Solid-State Sciences* vol 145, *Springer* (2005).

[5] A. M. Kadigrobov, R. I. Shekhter, S. I. Kulinich, M. Jonson, O. P. Balkashin, V. V. Fisun, Yu. G. Naidyuk, I. K. Yanson, S. Andersson and V. Korenivski: "Hot electrons in magnetic point contacts as a phonon source", *New Journal of Phys.* **13** (2011).

[6] Yu. G. Naidyuk, O. P. Balkashin, V. V. Finus, I. K. Yanson, A. M. Kadigrobov, R. I. Shekther, M. Jonson, V. Neu, M. Seifert, S. Andersson and V. Korenivski: "Stimulated emission and absorption of photons in magnetic point contacts: toward metal-based spin-lasers", *arXiv:11022167* (2011).

[7] R. I. Shekhter, A. M. Kadigrobov, M. Jonson, E. I. Smotrova, A. I. Nosich and V. Korenivski: "Subwavelength terahertz spin-flip laser based on a magnetic poin-contact array", *Optics Letters*, vol. 36, no. 12, pp. 2381-2383 (2011).

[8] A. M. Monakhov, V. V. Sherstnev, A. P. Astakhova, Yu. P. Yakovlev, G. Boissier et al.: "Experimental observation of whispering gallery modes in sector disk lasers", *Appl. Phys. Lett.* **94**, 051102 (2009).

[9] S. Andersoon: "Spin-Diode Effect and Thermally Controlled Switching in Magnetic spin-valves", *Doctoral Thesis in Physics at the KTH*, Stockholm, Sweden (2012).

[10] Albanova NanoFab Lab (KTH, Stockholm, Sweden) web-site (06/05/2012): *http://www.nanophys.kth.se/nanophys/facilities/nfl/maskaligner/maskalign.html.*

[11] M. Fischer: "Process Development for an Integrated Spin-Flip Laser Device", *Bachelor Thesis* at the Applied Physics department at KTH, Stockholm, Sweden (2011).

[12] K. Ellinas, A. Smyrnakis, A. Malainou, A. Tserepi and E. Gogolides: "'Mesh-assisted' colloidal lithography and plasma etching: A route to large-area, uniform, ordered nano-pillar and nanopost production on versatile substrates", *Microelectronic Engineering*, (2010).

[13] S. J. Moss: "Polymer degradation in reactive-gas plasmas", *Polymer Degradation and Stability*, vol. 17, iss. 3, pp. 205–222 (1987).

[14] A. Gromov: "Impedance of Soft Magnetic Multilayers: Application to GHz Thin Film Inductors", *Doctoral Thesis in Physics at the KTH*, Stockholm, Sweden (2001).

[15] Nanofabrication Center of the University of Minnesota (Minnesota, U.S.) web-site (06/05/2012): *http://www.nfc.umn.edu/photolithography/datasheet_ lor.pdf.*

[16] Albanova Nanostructures Physics department (KTH, Stockholm, Sweden) web-site (06/05/2012): *http://www.nanophys.kth.se/nanophys/facilities/nfl/resists/S1813/s1800seriesDataSheet.pdf.*

[17] A. Konovalenko: "Spin transfer torques and spin dynamics in point contacts and spin-flop tunnel junctions", *Doctoral Thesis in Physics at the KTH*, Stockholm, Sweden (2008).

[18] Y. Ji, C. L. Chien and M. D. Stiles: "Current-Induced Spin-Wave Excitations in a Single Ferromagnetic Layer", *Phys. Rev. Lett.*, vol. 90, num. 10, 106601 (2003).

[19] M. D. Stiles, J. Xiao and A. Zangwill: "Phenomenological theory of current-induced magnetization precession", *Phys. Rev. B* **69**, 054408 (2004).

[20] A. Konovalenko, V. Korenivski, I. K. Yanson and Yu. G. Naidyuk: "Spin-torque driven excitations and hysteresis in magnetic point contacts", *Journal of Appl. Phys.* **99**, 08G503 (2006).

[21] T. Y. Chen, Y. Li, C. L. Chien and M. D. Stiles: "Current-Driven Switching in a Single Exchange-Biased Ferromagnetic Layer", *Phys. Rev. Lett.*, vol. 93, num. 2, 026601 (2004).

[22] I. K. Yanson, Yu. G. Naidyuk, V. V. Fisun, A. Konovalenko, O. P. Balkashin, L. Yu. Triputen and V. Korenivski: "Surface Spin-valve Effect", *Nano Letters*, Vol. 7, No. 4, p. 927-931 (2007).

[23] A. Fert, I. A. Campbell: "Electrical resistivity of ferromagnetic nickel and iron based alloys", *J. Phys. F: Metal Phys.*, Vol.6, No.5 (1976).

[24] C. Vouille, A. Barthélémy, F. Elokan Mpondo and A. Fert, P. A. Schroeder, S. Y. Hsu, A. Reilly and R. Loloee: "Microscopic machanisms of giant magnetoresistance", *Phys. Rew. B*, Vol.60, No.9 (1999).